Zircons from Syros, Cyclades, Greece— Recrystallization and Mobilization of Zircon During High-Pressure Metamorphism

FRANK TOMASCHEK[1]*, ALLEN K. KENNEDY[2], IGOR M. VILLA[3], MARKUS LAGOS[1] AND CHRIS BALLHAUS[1]

[1]INSTITUT FÜR MINERALOGIE, WESTFÄLISCHE WILHELMS-UNIVERSITÄT MÜNSTER, CORRENSSTRAßE 24, D-48149 MÜNSTER, GERMANY

[2]CEMS, CURTIN UNIVERSITY OF TECHNOLOGY, PERTH 6845, W.A., AUSTRALIA

[3]INSTITUT FÜR GEOLOGIE, UNIVERSITÄT BERN, ERLACHSTRASSE 9A, CH-3012 BERN, SWITZERLAND

Zircons were studied from high-pressure/low-temperature metamorphosed meta-igneous lithologies from Syros. These rocks carry several zircon generations related to each other by dissolution–reprecipitation processes. One generation is pristine zircon that shows growth zoning, relatively elevated contents of trivalent cations and high Th/U ratios. The other end-member is a skeletal zircon generation with negligible trivalent cation contents and low Th/U ratios (≤ 0.1). Texturally between these two, there is a range of zircon crystals with complex inclusion populations of Y–HREE–Th phases and fluid inclusions, showing variable progress of replacement–recrystallization. Both end-members yield distinct sensitive high-resolution ion microprobe (SHRIMP) U–Pb ages. The pristine generation has an age of $80 \cdot 2 \pm 1 \cdot 6$ Ma from a metagabbro, and $76 \cdot 4 \pm 2 \cdot 1$ Ma from a meta-plagiogranite dyke. The skeletal, low-Th/U zircon generation yields an age of $52 \cdot 4 \pm 0 \cdot 8$ Ma. The older, Late Cretaceous, zircons are interpreted to date emplacement of the magmatic protoliths in a small segment of oceanic crust. The younger, Eocene, age, however, dates a zircon recrystallization event, which possibly coincides with high solubility and mobility of high field strength elements in a high-pressure aqueous fluid phase. Intergrowth relations between zircon and peak-metamorphic garnet, and excellent agreement of the U–Pb ages with white mica Ar–Ar ages for the same samples support the conclusion that Eocene is the true age of high-pressure metamorphism on Syros.

INTRODUCTION

The assessment of processes and parameters controlling zircon formation and stability is a challenging task and may provide information as to how zircon responds to metamorphism. Zircon is one of the most widely used minerals in geochronology. It incorporates small amounts of U and Th as well as other elements in solid solution (e.g. Speer, 1980; Hoskin *et al.*, 2000). Crystalline zircon is very capable of retaining the daughter products of radioactive decay as the diffusivity of ionic species is low (e.g. Cherniak *et al.*, 1997; Lee *et al.*, 1997), and the commonly observed resistance of near-end-member, non-metamict zircon toward geological processes is proverbial (Mezger & Krogstad, 1997). Zircon can form under nearly all geological conditions, including magmatic, hydrothermal, metasomatic, metamorphic (e.g. Rubin *et al.*, 1989; Claoué-Long *et al.*, 1990; Black *et al.*, 1991; Vavra *et al.*, 1996; Rubatto *et al.*, 1999; Liati & Gebauer, 1999), and possibly diagenetic (Saxena, 1966) processes. Therefore, some interest was focused on trace elements in solid solution that might be indicative of the

petrological history (e.g. Hoskin & Ireland, 2000; Rubatto, 2002).

Interpretation of ages obtained from zircon may not necessarily be straightforward. Geological interpretation of a U–Pb zircon age requires knowledge of the zircon-forming process, especially when zircon is the only datable mineral. The processes are often discussed with respect to metamorphic rims, interpreted either as overgrowths, where Zr is derived from an external source, or as *in situ* recrystallized domains (e.g. Pidgeon, 1992; Hanchar & Miller, 1993; Rubatto & Gebauer, 1999; Keay *et al.*, 2001). Metamictization resulting from accumulation of radiation damage is well established as a major variable controlling zircon susceptibility to alteration (e.g. Mezger & Krogstad, 1997; Geisler *et al.*, 2001). However, non-metamict zircon may also recrystallize (Pidgeon, 1992; Schaltegger *et al.*, 1999; Vavra *et al.*, 1999; Hoskin & Black, 2000) and may provide unique information on distinct petrogenetic episodes.

In this field-based study we document zircons from a dismembered meta-ophiolite sequence on the Cycladic island of Syros. The sequence forms part of the Cycladic Lower Unit and was overprinted in a high-pressure/low-temperature metamorphic event at blueschist- to eclogite-facies conditions. The principal aim is to address the geochronological problem of how zircon relates to oceanic crust formation and metamorphism. Geochronological and petrological methods were combined to overcome difficulties in determining the timing of zircon-forming events in HP/LT metamorphic rocks. Zircon generations were distinguished on textural and chemical grounds and were dated with sensitive high-resolution ion microprobe (SHRIMP). We describe zircon recrystallization textures, characterize the inferred dissolution–reprecipitation process, and attempt to correlate primary zircon growth and its subsequent remobilization with the petrological history of the rocks.

GEOLOGICAL BACKGROUND
Syros island is located in the centre of the Cycladic archipelago (Fig. 1) and forms part of the Attic–Cycladic Crystalline Complex (ACC) within the Hellenic orogen. The ACC may be characterized as a pile of tectonometamorphic units and is subdivided into a Lower Unit and an Upper Unit (Dürr, 1986). The Upper Unit consists of various klippen, predominantly of late Cretaceous (70–84 Ma) granitoids and low-pressure/high-temperature metamorphic rocks, as well as a variety of unmetamorphosed sediments (Reinecke *et al.*, 1982; Altherr *et al.*, 1994). The Lower Unit (LU) is composed of several tectonostratigraphic units. It includes pre-Alpidic basement,

marble–schist and volcanosedimentary sequences and slices of meta-ophiolite. The currently accepted Alpine tectonometamorphic evolution of the LU (see Okrusch & Bröcker, 1990) comprises (1) regional high-pressure blueschist–eclogite-facies metamorphism (M_1), at least Eocene in age; (2) a regional Oligocene to Miocene medium-pressure overprint (M_2); (3) a local contact metamorphic event (M_3) accompanying Miocene granitoid emplacement. Retrogression of the high-pressure rocks to greenschist-facies conditions either is related to decompression during exhumation or may reflect a distinct prograde metamorphic event. The medium-pressure overprint (M_2) is most prominent in the southern Cyclades (e.g. a migmatic dome on Naxos), whereas the high-pressure overprint (M_1) is best preserved on Sifnos, Tinos and especially Syros. Characteristic M_1 high-pressure assemblages on northern Syros comprise Jd + Pg + Qtz, Omp + Grt + Gln + Czo + Phg, Lws + Czo + Pg ± Qtz, as well as deerite-bearing amphibolite assemblages (Dixon, 1976; Bonneau *et al.*, 1980; Ridley, 1984; mineral abbreviations after Kretz, 1983). Constraints from limiting reactions agree with results from a multi-equilibrium approach (Trotet *et al.*, 2001), and indicate peak conditions at about 1·6 GPa and 480°C for the high-pressure metamorphic event on northern Syros.

PREVIOUS GEOCHRONOLOGY
Although the outlined geological evolution of the Lower Unit seems well established, there is debate about the age of the high-pressure (M_1) metamorphic event. Age information has come from K–Ar, Ar–Ar and Rb–Sr white mica geochronology (e.g. Altherr *et al.*, 1979, 1982; Andriessen *et al.*, 1979; Wijbrans & McDougall, 1986; Maluski *et al.*, 1987; Wijbrans *et al.*, 1990; Bröcker *et al.*, 1993; Baldwin & Lister, 1998) and recently from U–Pb zircon (Keay, 1998; Bröcker & Enders, 1999; Keay *et al.*, 2001). In addition, there have been attempts to constrain the metamorphic overprint with Ar–Ar on glaucophane (Maluski *et al.*, 1987), Sm–Nd on garnet (Seck *et al.*, 1996), and Lu–Hf on whole rock (Lagos *et al.*, 2002). White micas from high-pressure rocks of the Cycladic LU yield only one group of Eocene ages between 40 and 54 Ma. The available data indicate only one high-pressure metamorphic event, unlike mainland Greece, where Schermer *et al.* (1990) and Lips *et al.* (1998) have identified several distinct metamorphic episodes. The greenschist overprint (M_2) is dated with white mica to around 25–18 Ma (e.g. Altherr *et al.*, 1979; Wijbrans *et al.*, 1990; Bröcker *et al.*, 1993), in good agreement with U–Pb ages on zircon rims from the M_2 migmatic culmination on Naxos (21–17 Ma, Keay *et al.*, 2001). White mica ages obtained on Syros range from 36 to
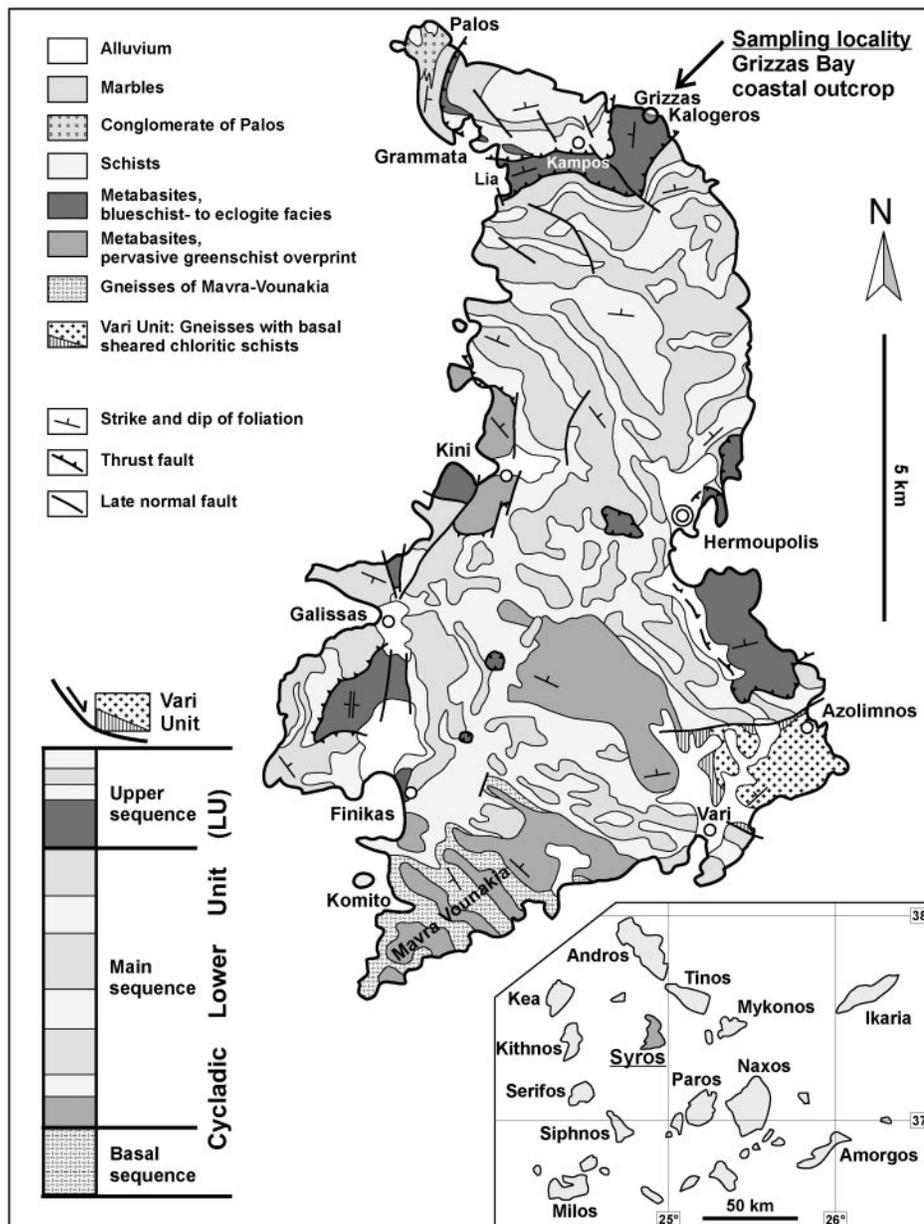
Fig. 1. Simplified geological map (based on Ridley, 1982; Hecht, 1984) and schematic tectonostratigraphic column of Syros. Sampling locality in the meta-ophiolite belt, coastal outcrop at Grizzas Bay, is indicated by the circle. Inset map shows the geographical location of Syros within the Cycladic archipelago.

54 Ma (Maluski *et al.*, 1987; Baldwin, 1996; Bröcker & Enders, 2001). The 50–54 Ma interval is regarded to be the most reliable age range for blueschist–eclogite-facies white micas, whereas the apparent younger ages result from partial retrogression (Baldwin, 1996).

Bröcker & Enders (1999, 2001) recently obtained a thermal ionization mass spectrometry U–Pb age of 78 ± 1 Ma on zircon crystals from meta-igneous rocks on Syros. Based on high-pressure minerals found in

some zircons, high field strength element (HFSE)-rich whole-rock compositions, and apparent agreement with metamorphic episodes established on mainland Greece, they interpreted their 78 ± 1 Ma age to date a Cretaceous high-pressure metamorphic event, implying a scenario of long-lasting subduction or multiple cycles of subduction from the Late Cretaceous to the Eocene. It should be noted, however, that this view is in conflict with other data and interpretations.

For example, for near-identical zircon crystals from Syros, Keay (1998) and Hoskin & Ireland (2000) obtained U−Pb ages and determined trace element contents using SHRIMP. Those workers interpreted their zircons with an age of 75 ± 2 Ma to reflect magmatic crystallization of the protolith. These conflicting interpretations motivate our work to assess the response of zircon and its relation to HP/LT metamorphism.

GEOLOGY OF SYROS

A simplified geological map of Syros is shown in Fig. 1. According to lithological criteria, Syros consists of three subunits, which form part of the Cycladic LU: (1) a basal sequence with metatuffaceous gneisses and schists, Ab + Ep + Act + Chl + Qtz greenstones, and metagranitic K-feldspar-bearing augen gneisses exposed in the south at Komito Bay; (2) a main schist–marble sequence in the central parts of the island, including metabasalts and ferromanganoan metasediments; (3) an upper sequence with metabasites, meta-plagiogranites, glaucophane schists, hydrothermal metasediments and minor schist–marble occurrences, best preserved in the north at Kampos and the coasts of the island around Kini and the city of Hermoupolis.

This lithological subdivision is supported by as yet unpublished SHRIMP U−Pb zircon ages (Keay, 1998; Tomaschek et al., 2001). The basal sequence contains metagranitoid K-feldspar augen gneisses of a Variscan (315 ± 3 Ma) protolith age; the main schist–marble sequence is of Mesozoic sedimentary age, locally interlayered with bimodal metatuffites (at Azolimnos) yielding late Triassic (243 ± 2 Ma) zircons; and the meta-igneous rocks at Kampos, described in this paper, give Late Cretaceous U−Pb zircon ages. The contacts between the units are tectonic and are probably thrusts developed during Eocene high-pressure deformation and rejuvenated during Miocene and younger extension (Ridley, 1982).

The Vari Unit, in the SE of Syros, rests upon a basal shear zone and consists of quartzofeldspathic gneisses, associated metabasites, schists and some intercalated marbles. SHRIMP U−Pb zircon ages for emplacement of granitoid orthogneiss protoliths are around 240−243 Ma (Keay, 1998; Tomaschek et al., 2001). Unlike the lithologies of the LU on Syros, these granitoids have not experienced Jd + Qtz stability, but recrystallized at epidote–amphibolite-facies conditions (Ridley, 1982), with $Ab_{(An08)}$ being a stable phase. The metamorphic overprint is of Cenomanian age, constrained from Ar−Ar and Rb−Sr white mica ages at 95−100 Ma (Tomaschek et al., 2000).

SAMPLING LOCATION

The samples of this study come from an association of metavolcanic rocks with metagabbro, located at Grizzas and Kalogeros. The lithologies constitute a large coherent block (~0·25 km^2 in outcrop), in the dismembered meta-ophiolite belt on northern Syros (e.g. Dixon & Ridley, 1987; Seck et al., 1996; Putlitz et al., 2000). According to field relations, the metavolcanic rocks form part of an extrusive, locally intrusive suite, comprising a complete compositional spectrum from mafic to felsic. During high-pressure metamorphism, the lithologies recrystallized to Gln + Omp + Czo ± Grt ± Phg metabasites, intermediate Gln + Grt-bearing Omp-pyroxenites, and Jd + Pg + Qtz ± Czo ± Phg felsites. At Grizzas, the metavolcanic suite is surrounded by static, cumulate-textured Omp−Czo metagabbro and as a result escaped penetrative deformation. Sharp primary lithological contrasts and emplacement structures are well preserved. Proximal breccia facies and more distal pillow equivalents are often in close proximity to each other and in association with hydrothermal metasediments. The mafic and felsic end-member compositions assembled in the volcanic breccias (Fig. 2a) also occur as intrusive dykes, sills and plugs in metagabbro (Fig. 2b), and the volcanic breccias carry metagabbro fragments as a common population of xenoliths. These observations suggest that the association (metavolcanic rocks with metagabbro) is a primary one and that the metavolcanic rocks post-date emplacement of the gabbro. We will present geochronological data obtained from the igneous-textured metagabbro, from a metamorphosed plagiogranite dyke cutting the metagabbro, and from a meta-plagiogranite breccia fragment in the metavolcanic rocks in direct contact with the gabbro; all sampled within 50 m in a coherent coastal outcrop in the SW of Grizzas Bay.

The geochemical history of the meta-igneous suite is complex and not yet fully understood. In many respects the meta-igneous suite preserves element abundances and signatures consistent with magmatic differentiation, such as decreasing TiO_2 and P_2O_5 with increasing silica content. Eu anomalies in chondrite-normalized rare earth element (REE) plots point to magmatic plagioclase fractionation and flat REE patterns are consistent with rocks formed in a back-arc environment (Kötz, 1989; Seck et al., 1996; Lagos et al., 2002). A decoupling of Zr and the middle REE (Sm, Nd) is not evidently related to the magmatic history. Postmagmatic changes in chemical composition are obvious in the alkali and alkaline earths, and a few erratic occurrences of high Zr contents of up to ~3000 ppm, which Bröcker & Enders (2001) attributed to high-pressure metamorphism.
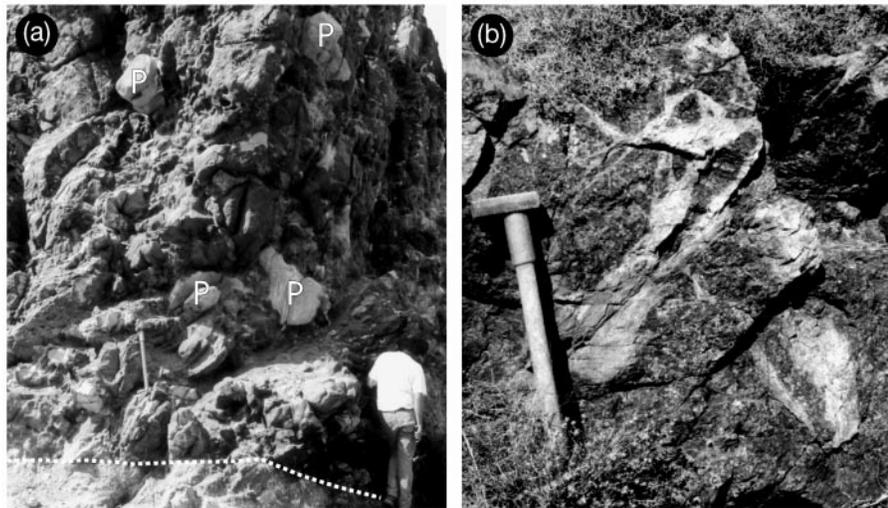
Fig. 2. Field relations of meta-igneous lithologies at the Grizzas–Kalogeros metagabbro. (a) Largely undeformed metavolcanic breccia, in direct contact with the metagabbro (below the dotted line). Several meta-plagiogranite fragments (P) occur as individual blocks in a metabasaltic matrix; coastal outcrop at Grizzas. (b) Meta-plagiogranitic dyke, intrusive in a pyroxenitic plug situated in undeformed metagabbro. The anastomosing veins and angular rafts of the coarse-grained darker matrix should be noted; inland outcrop near Kalogeros.

ANALYTICAL METHODS

Zircons were separated from sample sizes of about 4–15 kg. The rocks were crushed in a jaw crusher and the broken material was sorted on a Wilfley table for initial density separation. Further mineral concentration was carried out with a Frantz isodynamic magnetic separator and heavy liquids (bromoform, di-iodomethane). Finally, zircon crystals were hand-picked under a binocular microscope. About 40 zircon grains from each sample were mounted in epoxy along with chips of the reference standard zircon CZ3 (Pidgeon *et al.*, 1994), then polished. Back-scattered electron (BSE) and cathodoluminescence (CL) images, and electron microprobe analyses were obtained on carbon-coated surfaces. For isotopic SIMS analyses, samples were lightly repolished and coated with gold.

The BSE and CL images were obtained at 15 kV and 12 nA with a JEOL JXA 8900RL electron microprobe at the Institut für Geowissenschaften, Universität Mainz. Morphological features were imaged with secondary electrons (SE) at 20 kV and 1 nA with a JEOL JSM 840 scanning electron microscope at the Interdisziplinäres Centrum für Elektronenmikroskopie und Mikroanalyse (ICEM), Universität Münster.

Electron microprobe analyses were obtained with a JEOL JXA 8600 electron microanalyser at the ICEM, Universität Münster. Operating conditions were 20 kV and 30 nA. Counting times were 20 s for the major elements Zr-L_α (PET) and Si-K_α (TAP), and 60 s for Hf-M_α (TAP), Y-L_α (TAP), Yb-L_α (LIF) and P-K_α (PET), both on peak and background positions. As standards, synthetic materials were used, and data reduction was carried out with standard ZAF correction procedures.

Ion microprobe analyses for U, Th and Pb isotopes were obtained using the SHRIMP II at Curtin University of Technology, Perth. Spot sizes ranged between 20 and 30 μm, and the target areas were rastered before analysis. On each relevant magnetic field value, seven cycles were sampled with counting times optimized for the expected young U–Pb ages. The resultant time-integrated count rates were used to calculate isotopic ratios and the concentrations of U, Th and Pb for the analysis, following a similar approach to those used by Compston *et al.* (1984), Claoué-Long *et al.* (1995) and Williams *et al.* (1996). During each analytical session, systematic element fractionation was corrected for by using the correlation between ln(Pb/U) and ln(UO/U), obtained from a large number of standard analyses on the reference zircon CZ3, interspersed between unknown analyses at any analytical session. Errors cited in Table 2 (below) for individual analysis include errors from counting statistics and the U–Pb calibration error based on reproducibility of U–Pb measurements of the standard. Given the generally young zircon ages, U–Pb ages are calculated using the ^{207}Pb correction method (Compston *et al.*, 1984), which relies on an assumption of the isotopic composition of common Pb. Because, in a Tera–Wasserburg diagram, all samples with a single age plot on a mixing line toward common Pb of contemporaneous isotopic composition, the ratios according to the Cumming & Richards (1975) model were used to predict this
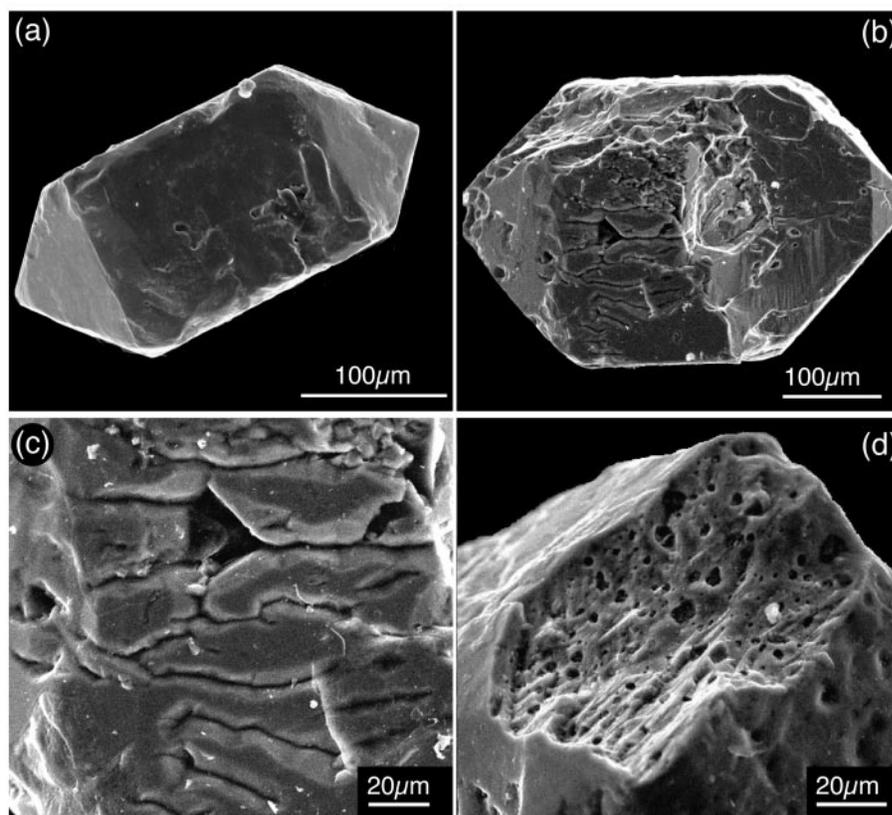
Fig. 3. Secondary electron images showing typical zircon morphologies from the Grizzas meta-plagiogranite samples. (a) Simple zircon habit, generally found for clear, pristine zircon crystals. (b) Grain morphology and (c) enlarged view of a zircon surface deeply cut by corrosion channels. (d) Detail on a broken edge of a euhedral, turbid, porous zircon (mechanical damage attributed to separation). The high density of voids (about 10 vol. % pores) should be noted; this was estimated from area exposure, and corresponds to fluid inclusions preserved in the interior of turbid crystals.

composition, $^{207}Pb/^{206}Pb = 0.838$, for an Alpine age. However, in most analyses the common Pb component ($f^{206}Pb$) is so low that calculated ages are largely insensitive to the assumed common Pb composition. Age calculations were performed using the Isoplot 2.06 software of Ludwig (1999) with the IUGS recommended constants (Steiger & Jäger, 1977). The mean population ages on grouped analyses were calculated from the concordia intersection of the regression line from common Pb. Isotopic ratios are plotted and mean ages are reported with an uncertainty of $\pm 2\sigma$.

Conventional Ar–Ar step heating experiments were carried out on visually pure paragonite separates. Aliquots of the separates were mounted for electron microprobe analysis. Samples of about 50 mg were irradiated with J value monitors at the research reactor in Risø, Denmark, and degassed at steps typically lasting 20 min, in a vacuum resistance oven connected to a MAP 215-50B mass spectrometer at the Universität Bern. A detailed description of the analytical procedures and of interference corrections has been given by Belluso *et al.* (2000). Results are listed with internal errors resulting from in-run statistics, including uncertainties on interference corrections. The complete dataset is available for downloading from the *Journal of Petrology* web site at http://www.petrology.oupjournals.org.

ZIRCON MORPHOLOGY AND INTERNAL STRUCTURES

Zircons from the blueschist–eclogite facies metamorphosed samples comprise texturally complex populations. Types of zircon from the mineral separates are illustrated in Figs 3–6. The subdivisions used here are based on crystal morphology, degree of alteration, porosity and inclusion population. We distinguish clear pristine zircons (type 1), composite zircons with domains of relict pristine zircon (type 2), turbid porous zircons rich in inclusions (type 3) and skeletal zircons (type 4).

Pristine (type 1) zircons are clear, colourless, medium to short prismatic and euhedral in shape. The crystal morphology (Fig. 3a) shows a combination of
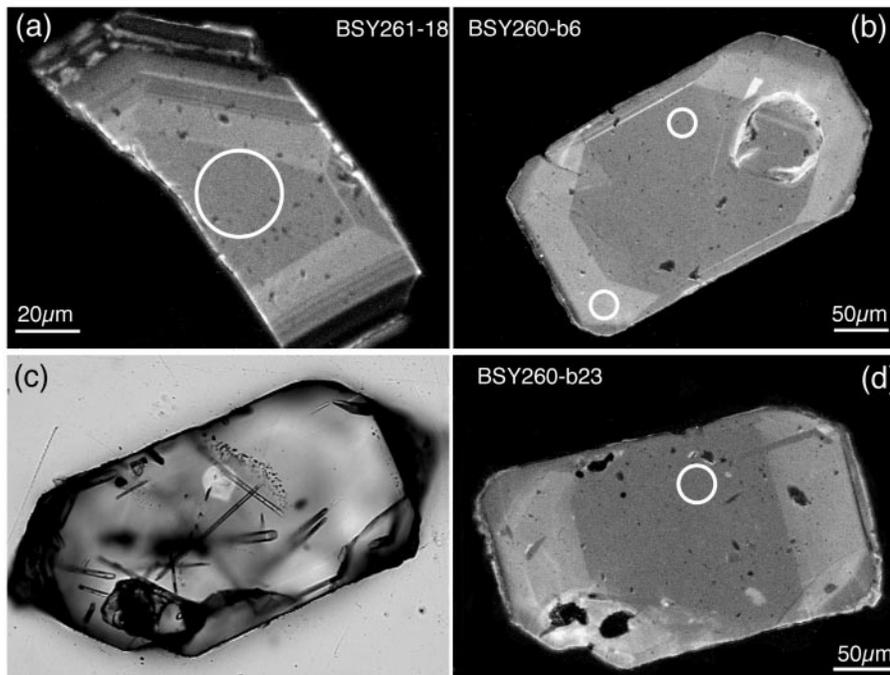
Fig. 4. Internal textures of clear, pristine zircons (type 1) from the metagabbro sample (BSY261) and the meta-plagiogranite dyke (BSY260). Circles indicate areas of SHRIMP analyses; numbers correspond to codes in Table 2. (a) Cathodoluminiscence (CL) image of a zircon from the metagabbro showing oscillatory and sector zoning. The bright luminescent, altered patches in the outer, dark, trace element enriched growth zones should be noted. (b) CL image of a zircon from the plagiogranitic dyke sample. Despite two growth zones and sector zoning, the zircon appears nearly homogeneous in CL image; area of enhanced luminosity around a crack. (c) Transmitted light image of zircon from the meta-plagiogranite dyke and (d) the corresponding CL image. The randomly oriented apatite needles, interpreted to be primary magmatic inclusions, as well as trails of secondary fluid inclusions, should be noted. The rectangular feature in the lower left might have been a primary silicate inclusion, now polyphase, and with disturbed luminosity in the adjacent zircon.

the $\{100\}$ tetragonal prism and the $\{101\}$ tetragonal bipyramid (X-ray setting). Many type 1 crystals show signs of resorption. Compared with the other zircon types, however, crystal faces tend to be smooth and less corroded. In CL image, internal structures are simple. Most of the pristine type 1 zircon grains have relatively few growth zones, although some specimens of the metagabbro sample exhibit pronounced oscillatory growth zoning (Fig. 4a and b). The only primary inclusions observed are apatite needles (Fig. 4c). The pristine zircon generation is most frequent in the metagabbro sample and the meta-plagiogranite dyke in metagabbro; these rock types best preserved original magmatic textures.

Composite (type 2) zircons also show euhedral shapes but their crystal faces tend to be more intensively pitted and cut by resorption channels (Fig. 3c). In CL and BSE image, the type 2 zircon crystals consist of a porous, sometimes spongy rim around relict domains of pristine zircon. The altered domains appear bright and patchy in CL image, and domain boundaries toward pristine cores are irregularly curved (Fig. 5b and d). The most frequent types of inclusions

in the porous rims are fluid inclusions (preserved in the interior of the crystals and represented by voids in SE and BSE images), xenotime, and Y–heavy REE (HREE)–Th silicate phases. Type 2 zircon crystals are observed in all lithologies.

Porous (type 3) zircons are distinguished from the type 2 generation by lack of pristine cores and a more pervasive state of alteration. Type 3 zircon grains still have euhedral shapes although crystal faces are highly irregular and strongly pitted. The porous crystals are milky white to pale brownish orange. In transmitted light, these grains are nearly opaque as a result of the high density of inclusions and pores (Figs 3d and 6a). These crystals are not suspected to be metamict, despite their appearance. In specially prepared ultrathin sections ($\sim$5–8 μm) they show normal birefringence and uniform extinction. Single-crystal X-ray diffraction (XRD) analyses of porous zircon grains gave lattice parameters characteristic for near-end-member, non-metamict zircon [e.g. $a = 6\cdot609(2)$ Å, $c = 5\cdot983(2)$ Å, compared with the values of $a = 6\cdot607(1)$ Å, $c = 5\cdot982(1)$ Å from Robinson *et al.* (1971)]. Inclusion populations are two-phase water

1983
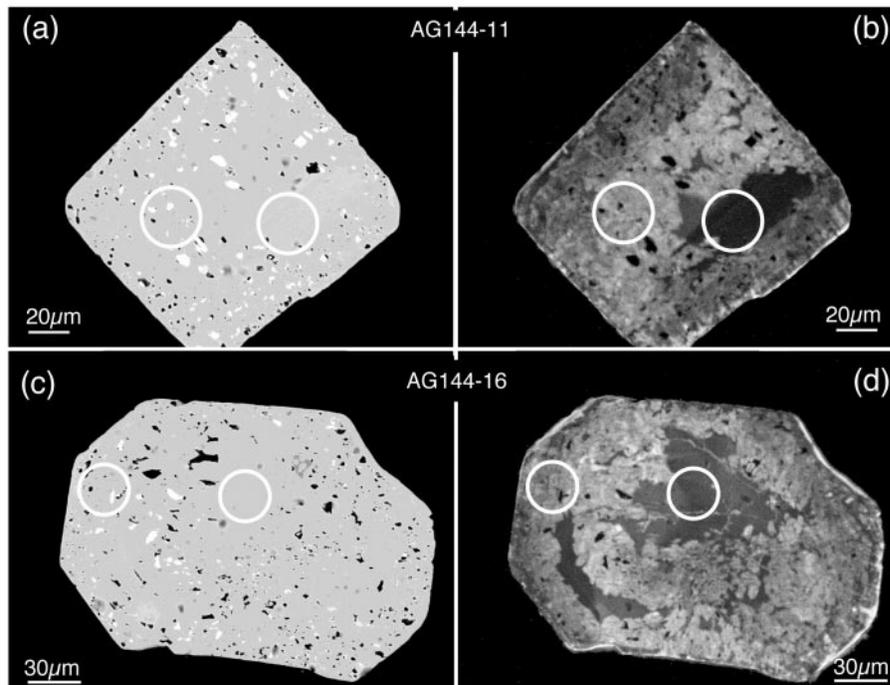
Fig. 5. Internal textures in BSE (left column) and CL images (right column) of zircons from the plagiogranitic fragment in the Grizzas breccia (AG144). Areas targeted with SHRIMP are circled, and codes correspond to results in Table 2. (a)–(d) Complex, partially altered zircons (type 2). Relict domains show low luminosity and are homogeneous in BSE image. Altered domains appear bright in CL image and are rich in inclusions. Dark spots in BSE image are voids of fluid inclusions; bright spots are Y–REE–Th-rich phases.
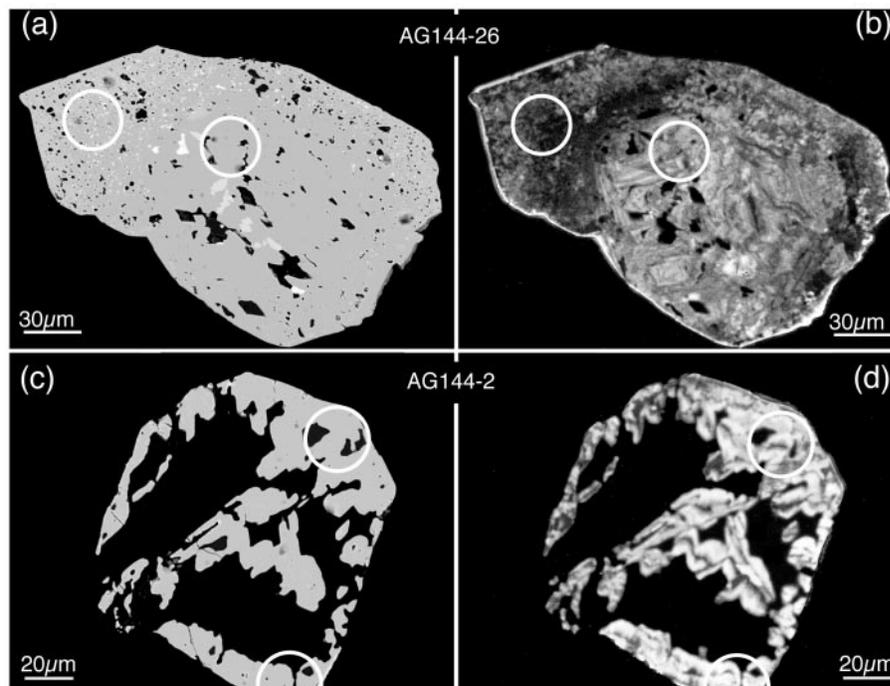
Fig. 6. (a) BSE and (b) CL images of completely altered zircons of the inclusion-rich porous type 3 generation (see text). Outer shell with fine-grained inclusions, around a discrete inner domain that corresponds to the skeletal generation. In the inner dense domain, noteworthy features are the curved phase boundaries, some fluid voids and channels, and intergrowths with silicate phases (predominantly quartz) in several of the larger areas, dark in BSE image. Y–HREE–Th inclusions appear bright in BSE image. (c) BSE and (d) CL image of a skeletal (type 4) zircon. Irregular CL intensities outline zircon boundaries. The dark intergrown phase is quartz.

and gas-rich fluid inclusions, xenotime, Y–HREE–Th silicate phases, and some apatite. Individual zircon crystals show transitions between highly porous and dense domains, distinguished with respect to distribution of inclusions, shape of phase boundaries and appearance in CL (Fig. 6a and b).

Skeletal (type 4) zircons show hollow shapes in CL and BSE image (Fig. 6c and d) and tend to be free of fluid inclusion voids. These zircon crystals also lack Y–HREE–Th phase inclusions and are found intergrown with peak metamorphic silicate phases. The type 4 zircons are generally encountered together with the porous, type 3 zircons. Both types predominate in the most recrystallized, plagiogranite fragments of the metavolcanic breccia. Skeletal zircon presumably represents an end-member of the recrystallization process, as described below.

ZIRCON MINERAL CHEMISTRY

The composition of natural zircon can be very complex. With respect to the most important elements, the formula may be given as $(Zr,Hf,Y,HREE,U,Th)$-$(Si,P)O_4$. Many other elements, including alkali and alkaline earths, various transition elements, and hydrous species, may substitute in the zircon structure (e.g. Speer, 1980; Hoskin *et al.*, 2000; Hanchar *et al.*, 2001). In this study, zircons analysed for trace elements were first scanned qualitatively to define target elements and to identify textural and chemical domains for later quantitative electron microprobe analysis.

Elemental distribution maps on composite grains may provide some clues to the origin of porous zircon. Figure 7a and b illustrates in BSE and CL images a typical example of a type 2 composite zircon with well-developed primary and secondary features. A porous, fluid inclusion-rich outer shell surrounds a smooth, pristine domain in the centre (Fig. 7a). The CL image (Fig. 7b) shows a minor rim and alteration transecting primary textures, leaving behind isolated domains of pristine zircon. It also reveals a sector zonation present in the pristine core. In the corresponding element maps (Fig. 7c), Zr and Hf abundances decrease from centre to edge whereas Y (and presumably trivalent REE) increase. In the example shown, low Y in the centre and elevated Y in the enriched growth zone correspond to about 1 and 3 wt % Y_2O_3, respectively. In the porous rim, some zircon domains, notably those with fluid inclusion voids, have near-end-member compositions, evident from maximum Zr and minimum Y intensities. Near-pure zircon domains coexist with discrete Y and Th phases that show up as bright areas in the

corresponding BSE image in Fig. 7a. A close comparison of the Y and P element maps also reveals that at least two different Y phases must be present, of which one is xenotime, $(Y,HREE)PO_4$, and the other a poorly characterized Y–HREE–Th silicate, perhaps keiviite, $(Y,HREE)_2Si_2O_7$. The presence of discrete Th phases in the porous shell was only verified by energy dispersive analysis. It is evident that during recrystallization of type 1 zircon to form the porous zircon shell, trace elements such as Y, Th, P and the REE were expelled from the zircon structure and precipitated *in situ* as discrete phases.

Quantitative analyses were collected on magmatic and metamorphic zircon from a wide range of lithologies on Syros, of which a representative subset is given in Table 1. In Fig. 8, the trivalent cations represented by Y and Yb are shown against the pentavalent cation P. This figure shows absolute concentrations and provides information on charge balancing. The highest concentrations in trivalent cations are encountered in the pristine (type 1) zircon generation, with 2–3 wt % R_2O_3 in the plagiogranite and metagabbro zircons. Among these, the zircons from the igneous-textured metagabbro sample are most enriched in trace elements. Recrystallization of the type 1 zircon generation leads to a significant loss of Y and Yb from the structure, and appears to be accompanied by *in situ* precipitation of xenotime and Y–HREE–Th silicates, as already suggested from the element distribution maps (Fig. 7c) and represented by the inset in Fig. 8a. Area scan analyses on porous, inclusion-rich zircon domains, to reintegrate zircon and coexisting Y–HREE–Th phases, give bulk compositions that are reasonably similar to those of relict pristine zircon (grey-line envelope in Fig. 8b). This suggests that differential transport of minor elements, following expulsion from the zircon structure, was minimal in many cases. The lowest concentrations in trivalent cations and phosphorus are encountered in the skeletal (type 4) zircon generation. Analyses obtained on the complex porous zircon domains, coexisting with xenotime, do not yield more than about 1 mol % xenotime component, and some of the highest values may well represent partial mixtures of zircon with xenotime inclusions.

Figure 8 also shows that the trivalent cations are not fully charge-balanced by P^{5+}. Indeed, there are two arrays in $(Y + Yb)/P$ atomic ratio, one array with a slope of ~ 4, and the other $\sim 1 \cdot 4$, closely approaching the xenotime exchange vector with $(Y + Yb)/P = 1$. It is often recognized from zircon analyses that the xenotime exchange, $Y^{3+} P^{5+} Zr^{4+}_{-1} Si^{4+}_{-1}$, is not the exclusive substitution to account for Y and HREE in the zircon structure (e.g. Hinton & Upton, 1991; Finch *et al.*, 2001). The differences in $(Y + Yb)/P$ may reflect the bulk chemistries of the samples: all analyses with
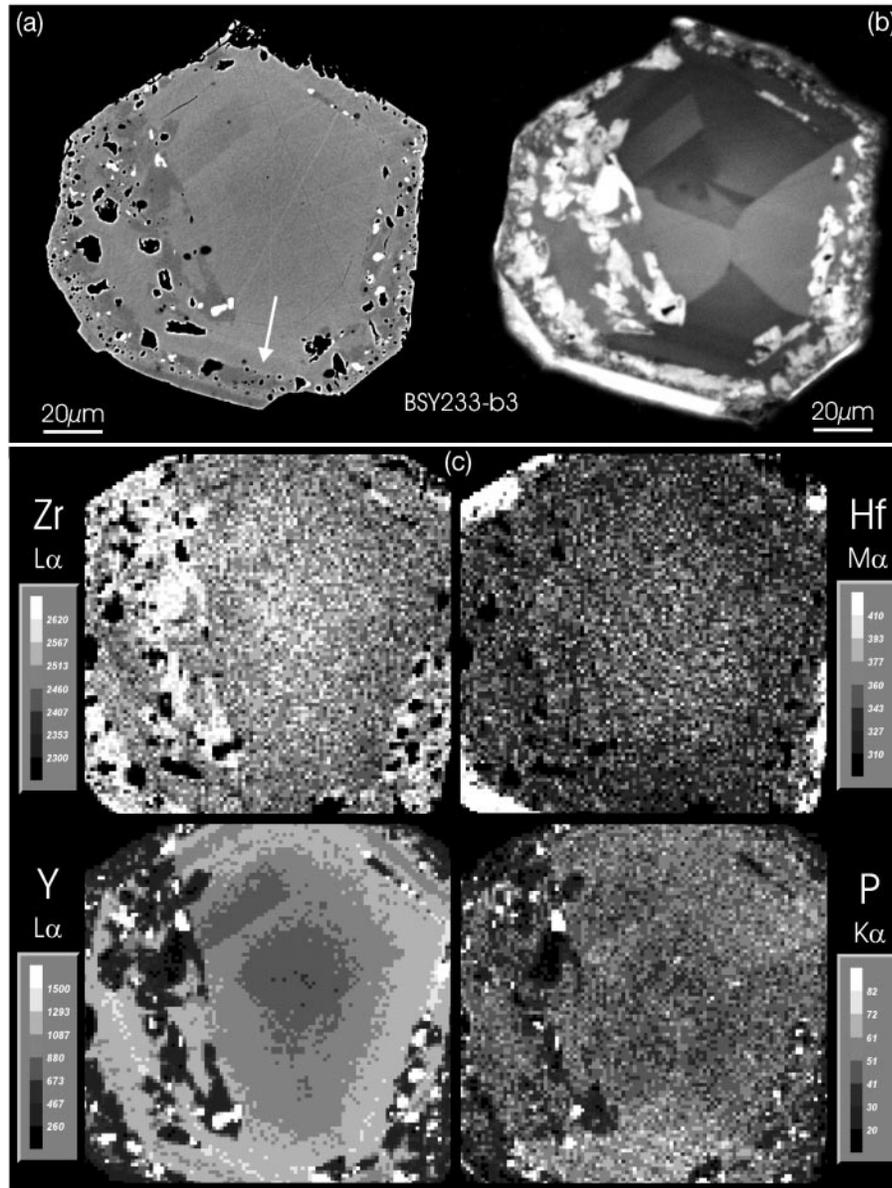
Fig. 7. A complex type 2 zircon (see text) from a leucocratic metatuffaceous layer at Azolimnos in the SE of the island (Fig. 1). (a) BSE and (b) CL images show a homogeneous, pristine core and porous, inclusion-rich domains along the peripheries. Altered, inclusion-rich zircon domains and an external rim show brighter luminosity. Bright spots in BSE image correspond to Y–HREE–Th-rich phases; dark areas are fluid inclusion voids. Arrow points to a group of pores at the interface between different zircon domains. (c) Element distribution maps for Zr-L_α, Hf-M_α, Y-L_α and P-K_α of the complex zircon, with grey shades reflecting count rates. Decreased contents of P and Y characterize recrystallized zircon in the altered domains. It should be noted that Y and P intensities do not fully overlap, suggesting the presence of at least two different Y-rich phases.

$(Y + Yb)/P \sim 4$ are from silica-saturated, highly differentiated lithologies in which P_2O_5 is close to the detection limit, whereas the zircons following $(Y + Yb)/P \sim 1{\cdot}4$ are derived from the mafic metagabbro sample. Charge balance mechanisms for the low-phosphorus zircon must remain speculative. Although various trace elements may effectively assist in charge balance (e.g. Hoskin *et al.*, 2000), no additional cations were found in significant amounts. It is possible, however, that the apparent deficit in P^{5+} is compensated by cations such as Li^+ or even hydroxyl groups replacing O^{2-} (e.g. Woodhead *et al.*, 1991; Hanchar *et al.*, 2001), both of which are not detectable with conventional electron microprobe analysis.

Table 1: Representative electron microprobe analyses of zircons from Syros

Sample	BSY233 felsic metatuffaceous layer, Azolimnos					BSY261 metagabbro, Grizzas				
	4-2-PRI	3-2-PRI	3-8-PRI	3-10-PD	3-11-rim	5-2-PRI	19-1-PRI	18-7-PRI	17-10-PRI	17-14-PRI
wt %										
SiO_2	33·22	32·67	32·29	33·10	33·26	33·13	32·98	32·80	32·32	31·96
ZrO_2	65·40	64·07	61·92	65·61	65·37	65·39	64·38	63·47	61·59	60·87
HfO_2	1·64	0·97	0·85	0·96	1·33	1·36	1·02	1·84	2·66	3·16
Y_2O_3	0·12	1·25	2·56	0·13	0·08	0·13	0·78	0·88	1·60	2·07
Yb_2O_3	0·12	0·08	0·81	0·00	0·19	0·00	0·00	0·30	0·44	0·36
P_2O_5	0·08	0·31	0·51	0·08	0·12	0·06	0·16	0·51	0·83	1·07
Sum	100·58	99·35	98·94	99·87	100·35	100·07	99·31	99·80	99·42	99·48
p.f.u.										
Si	1·011	1·005	1·002	1·011	1·012	1·011	1·013	1·006	0·999	0·990
Zr	0·970	0·961	0·937	0·977	0·970	0·973	0·964	0·949	0·928	0·919
Hf	0·014	0·009	0·008	0·008	0·012	0·012	0·009	0·016	0·023	0·028
Y	0·002	0·020	0·042	0·002	0·001	0·002	0·013	0·014	0·026	0·034
Yb	0·001	0·001	0·008	0·000	0·002	0·000	0·000	0·003	0·004	0·003
P	0·002	0·008	0·013	0·002	0·003	0·002	0·004	0·013	0·022	0·028
Sum	2·000	2·003	2·009	2·000	2·000	2·000	2·002	2·001	2·002	2·002

	BSY260 meta-plagiogranite dyke, Grizzas				AG144 meta-plagiogranite breccia fragment, Grizzas					
	18-5-PRI	18-2-PRI	18-4-PRI	4-4-PRI	16-3-PRI	5-3-PP[*]	5-1-PD	5-2-PD	27-1-SK	27-2-SK
wt %										
SiO_2	33·33	33·23	33·19	32·99	32·62	31·94	33·01	32·88	33·15	32·85
ZrO_2	65·79	65·36	65·00	64·94	62·15	61·68	65·34	65·20	66·08	65·48
HfO_2	1·10	1·03	1·03	1·01	0·95	1·05	0·97	0·92	1·10	1·25
Y_2O_3	0·17	0·37	0·68	0·91	2·08	2·30	0·21	0·47	0·00	0·32
Yb_2O_3	0·00	0·28	0·32	0·68	0·85	0·10	0·23	0·22	0·00	0·00
P_2O_5	0·07	0·15	0·14	0·17	0·33	0·45	0·13	0·31	0·02	0·23
Sum	100·46	100·41	100·35	100·70	98·98	97·52	99·88	100·00	100·34	100·13
p.f.u.										
Si	1·012	1·011	1·011	1·005	1·010	1·002	1·009	1·004	1·009	1·003
Zr	0·974	0·969	0·965	0·965	0·939	0·944	0·974	0·971	0·981	0·975
Hf	0·010	0·009	0·009	0·009	0·008	0·009	0·008	0·008	0·010	0·011
Y	0·003	0·006	0·011	0·015	0·034	0·038	0·003	0·008	0·000	0·005
Yb	0·000	0·003	0·003	0·006	0·008	0·001	0·002	0·002	0·000	0·000
P	0·002	0·004	0·004	0·004	0·009	0·012	0·003	0·008	0·000	0·006
Sum	2·000	2·001	2·003	2·004	2·008	2·007	2·001	2·000	2·000	2·000

Analyses codes give PRI (pristine domain), PP[*] (inclusion-rich porous domain; [*]area scan analysis), PD (dense domain in porous zircon) and SK (skeletal domain) according to zircon textures. Atoms per formula unit (p.f.u.) calculated from normalization to four oxygens.

Another important aspect is the presence of pristine zircon analyses with very low trace element contents. In Fig. 8a this population is represented by several filled symbols very near the origin of the diagram. These zircons do not show any signs of recrystallization. We will point out in the Discussion that these zircons remained pristine because of low trace element content, similar to conclusions
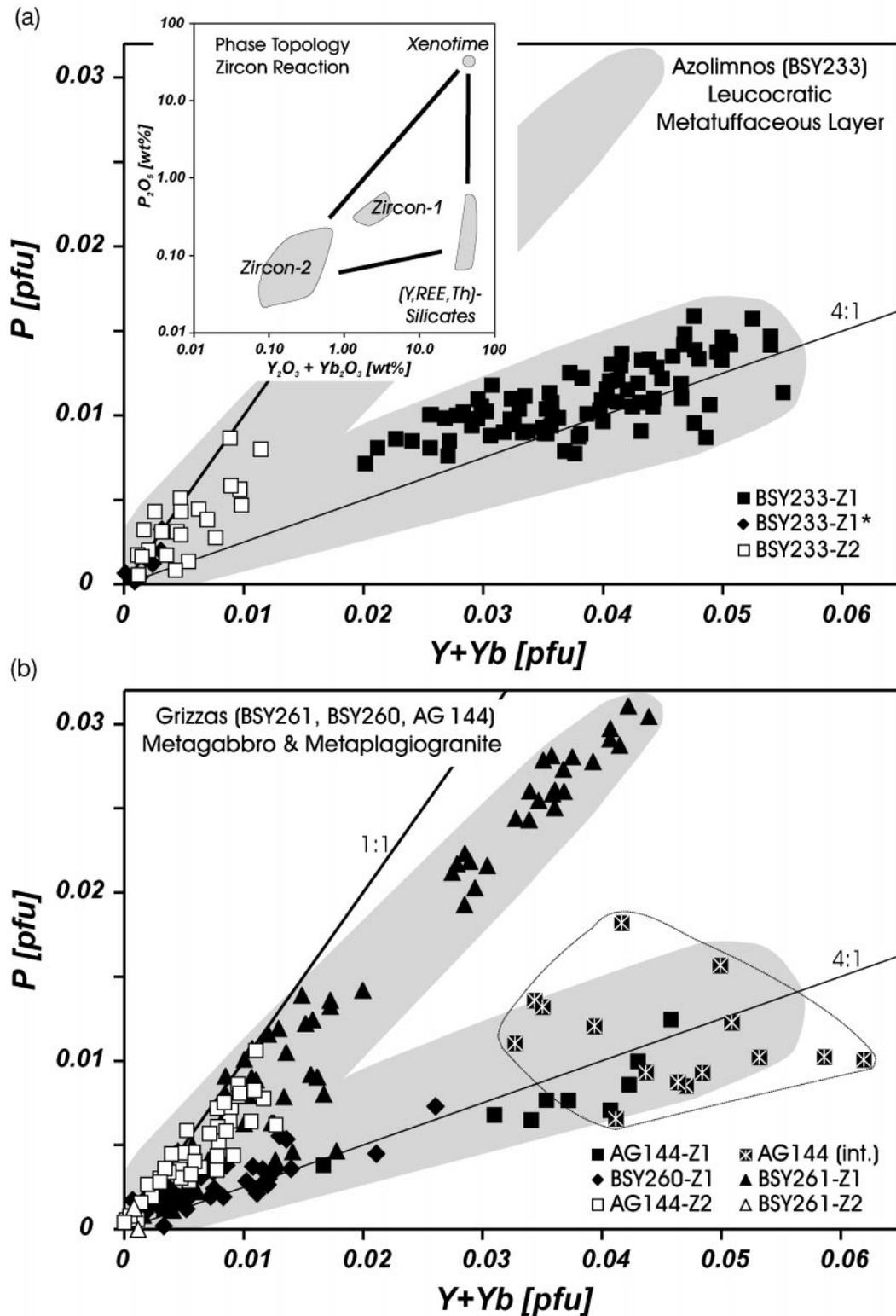
Fig. 8. Correlation between Y + Yb and P cations per zircon formula unit (see Table 1). Bold line indicates ideal xenotime substitution trend. Filled symbols denote analyses obtained on pristine (type 1) zircon; open symbols recrystallized domains and overgrowth rims. (a) Zircon analyses from the Azolimnos sample (Fig. 7); recrystallization decreases concentrations in trivalent cations and P. Inset graph represents the zircon reaction, including partial analyses of inclusion phases. (b) Zircons from the meta-igneous samples at Grizzas falling along the xenotime substitution and a P-poor trend. Grey-line envelope encloses reintegrated area scan analyses on porous, inclusion-rich zircon domains.

drawn by Köppel & Sommerauer (1974) and Hoskin & Black (2000).

SHRIMP U–Th–Pb RESULTS

Ion microprobe analyses were carried out on zircon grains previously imaged by BSE and CL. Results are given in Table 2 and plotted in Tera–Wasserburg diagrams (Figs 9 and 10).

Metagabbro

The metagabbro sample yielded mostly pristine zircon crystals (Fig. 4) with broad or oscillatory growth zonation. No optically distinct cores were observed. Recrystallization in the form of porous zircon is minor and confined to narrow rims. Additional minor disturbance is obvious from enhanced luminosity along inclusions or brittle cracks. Some specimens show cracks that are sealed with a low-luminescence, secondary zircon generation, whereas other grains have narrow bright luminescent overgrowth rims. Neither the crack sealing nor the metamorphic rims were large enough for contamination-free SHRIMP analysis.

For the metagabbro sample, 12 spot analyses were collected on pristine zircon domains from eight zircon grains. In the Tera–Wasserburg diagram (Fig. 9a), the U–Pb data form a tight array extending back to common Pb. One outlier, obtained on an external bright luminescent zone, has very low U content and exceptionally high f^{206}Pb, and is excluded from the age calculation as secondary disturbance is likely. The well-defined regression line in Fig. 9a gives an age of $80\cdot2 \pm 1\cdot6$ Ma (2σ, $n = 11$, MSWD $= 0\cdot3$). In the Discussion, we conclude that this age dates magmatic crystallization of the protolith.

Meta-plagiogranite dyke

Zircons from the metamorphosed plagiogranite dyke (cutting the metagabbro) are similar in morphology and internal texture to those from the metagabbro, although they lack oscillatory zoning (Fig. 4). Fifteen analyses were carried out on pristine domains of 12 grains. One analysis, presumed to be contaminated with secondary zircon along a young crack, yields the highest U and Th contents (200 and 262 ppm, respectively) and youngest age, and is therefore excluded from the regression. The scatter in Fig. 9b is clearly too large for a single homogeneous zircon population, although CL imaging did not reveal any distinct cores or other textures in the spots analysed. Analyses of internal and external growth zones of single zircon grains are the same within error. The single spot results range in age from 73 to 91 Ma, with Th/U ranging from 0·3 to 1·1. The Th/U ratio and apparent ages are not correlated, so a single secondary process is unlikely to account for the wide scatter. The populations are divided based on their ages (Fig. 9b). Regression of the main group yields an age of $76\cdot4 \pm 2\cdot1$ Ma (2σ, $n = 12$, MSWD $= 2\cdot5$), whereas the second group gives an age of $88\cdot5 \pm 3\cdot9$ Ma (2σ, $n = 2$, MSWD $= 1\cdot8$). Below we suggest that the younger age dates the plagiogranite dyke intrusion whereas the scattered older ages might represent an inherited zircon component.

Meta-plagiogranite breccia fragment

The zircons recovered from a meta-plagiogranite fragment of the metavolcanic breccia mostly belong to the recrystallized generation. Therefore, SHRIMP analyses targeted individual domains, identified from previous BSE and CL imaging. The results of 19 analyses obtained on 14 grains are listed in Table 2 and illustrated in Fig. 10. The analytical data are coded according to the textural domains defined from the images (Figs 5 and 6).

A wide spread of ages is obtained, ranging from 84 to 32 Ma. In general, pristine-looking domains are older than porous and skeletal domains. The two oldest ages on relict pristine domains are *c.* 82 Ma, and accord well with results from pristine zircon of the metagabbro and the plagiogranitic dyke samples (Fig. 10b). Analyses of porous domains scatter widely in age and Th/U. The scatter may be due to (1) variable Pb loss postdating recrystallization or reflecting incomplete resetting during recrystallization, (2) sampling of multiple zircon domains, or (3) analytical bias owing to inclusions smaller than spot resolution.

Seven analyses of skeletal zircons together with some domains of the porous zircon generation fall along a tight regression line in Fig. 10a, and give ages between 50 and 53 Ma. These samples have the lowest Th/U ratios ($\leq 0\cdot12$; Fig. 10b), deemed characteristic for metamorphic zircon (e.g. Williams & Claesson, 1987; Rubatto, 2002). The skeletal and low-Th/U zircons form a tight group in the age–Th/U correlation diagram [Fig. 10b; see also fig. 3 of Hoskin & Black (2000)]. This leads us to suggest that these zircons give a geologically meaningful age of $52\cdot4 \pm 0\cdot8$ Ma (2σ, $n = 7$, MSWD $= 0\cdot9$). Below we consider that this age may date high-pressure peak metamorphism.

DISCUSSION

This section will discuss the age and genesis of type 1 zircon (pristine zircon generation) and the process of recrystallization that relates type 1 zircon to the other (porous and skeletal) zircon generations. The discussion will take into account the geological

Table 2: Ion microprobe U–Th–Pb data for zircons from Grizzas, Syros

Sample	U (ppm)	Th (ppm)	Th/U	Pb (ppm)	$f^{206}Pb$ (%)	$^{238}U/^{206}Pb \pm 1\sigma$ (measured)		$^{207}Pb/^{206}Pb \pm 1\sigma$ (measured)		Age (Ma) $\pm 1\sigma$ (207-corrected)	
BSY261 igneous-textured metagabbro, pristine zircon domains											
261-2i	62	41	0·67	1	20·1	64·721	2·329	0·2068	0·0124	79·1	3·2
261-4i	21	13	0·60	1	37·0	50·246	2·701	0·3399	0·0257	80·3	6·0
261-4e/x	12	5	0·39	0	52·0	58·055	4·183	0·4587	0·0436	53·0	7·2
261-10i	26	17	0·68	1	33·1	51·554	2·746	0·3091	0·0237	83·1	5·8
261-16i	264	318	1·20	5	5·5	76·243	1·575	0·0911	0·0039	79·4	1·7
261-18i	250	180	0·72	4	4·5	76·307	1·683	0·0829	0·0041	80·2	1·8
261-19i	43	34	0·79	1	21·0	60·456	2·642	0·2132	0·0153	83·7	4·2
261-24c1	69	41	0·60	1	16·1	66·975	2·252	0·1747	0·0103	80·3	3·0
261-24c2	77	49	0·63	2	14·2	68·852	2·200	0·1596	0·0093	79·9	2·8
261-24e	94	61	0·65	2	8·1	72·854	2·245	0·1118	0·0073	80·8	2·6
261-26i	81	59	0·72	2	15·0	69·522	2·228	0·1660	0·0096	78·4	2·7
261-26e	52	17	0·33	1	17·0	64·107	2·503	0·1819	0·0127	82·9	3·6
BSY260 meta-plagiogranite dyke in metagabbro, pristine zircon domains											
260-a4	109	91	0·83	2	5·8	66·002	2·095	0·0937	0·0063	91·4	3·0
260-a5	143	152	1·06	2	5·1	75·700	1·977	0·0881	0·0042	80·3	2·1
260-a12	140	125	0·89	2	9·9	80·606	2·183	0·1258	0·0055	71·7	2·0
260-a13	83	64	0·77	2	7·7	68·747	2·023	0·1082	0·0056	86·0	2·6
260-a14	103	82	0·80	2	9·8	73·627	2·087	0·1251	0·0058	78·5	2·3
260-a20/x	220	262	1·19	3	6·1	93·041	2·285	0·0960	0·0039	64·7	1·6
260-b2i	72	49	0·69	2	18·7	70·442	1·697	0·1954	0·0080	74·0	2·0
260-b2e	47	15	0·32	1	16·9	70·817	2·106	0·1816	0·0097	75·2	2·5
260-b6i	53	34	0·65	1	15·7	65·595	1·756	0·1715	0·0083	82·3	2·4
260-b6e	38	17	0·45	1	16·5	66·098	2·027	0·1782	0·0099	80·9	2·8
260-b7i	118	94	0·79	2	12·1	76·080	1·551	0·1432	0·0055	74·0	1·6
260-b7e	47	22	0·47	1	13·2	72·354	2·099	0·1516	0·0087	76·9	2·4
260-b24i	68	46	0·68	1	13·4	72·669	2·012	0·1534	0·0082	76·4	2·3
260-b19i	67	47	0·70	1	16·7	68·804	1·624	0·1800	0·0073	77·5	2·0
260-b23i	120	97	0·81	2	8·4	80·083	1·591	0·1140	0·0046	73·3	1·5
AG144 meta-plagiogranite volcanic breccia fragment											
144-2 s (SK)	282	13	0·04	3	15·5	109·182	3·016	0·1705	0·0089	49·6	1·5
144-2s2 (SK)	533	13	0·02	5	3·7	116·185	2·349	0·0767	0·0035	53·2	1·1
144-3 s (PD)	396	28	0·07	4	6·4	112·372	2·210	0·0981	0·0039	53·4	1·1
144-4 s (PP)	290	256	0·88	5	20·8	92·696	1·933	0·2116	0·0068	54·8	1·3
144-5 s (PP)	763	533	0·70	10	5·1	100·634	1·610	0·0880	0·0025	60·5	1·0
144-6p (PRI)	454	534	1·18	7	7·0	86·214	1·553	0·1027	0·0034	69·2	1·3
144-6 s (PP)	350	116	0·33	4	22·5	155·255	3·543	0·2252	0·0082	32·1	0·8
144-11p (PRI)	1005	1746	1·74	19	1·9	75·103	1·100	0·0623	0·0016	83·7	1·2
143-11 s (PP)	440	237	0·54	5	7·1	110·144	2·111	0·1036	0·0039	54·1	1·1
144-12 s (PD)	581	69	0·12	5	3·4	117·938	2·086	0·0746	0·0029	52·5	0·9
144-15 s (PD)	464	39	0·08	4	6·8	113·417	2·122	0·1010	0·0037	52·7	1·0
144-16p (PRI)	598	630	1·05	10	4·7	76·911	1·272	0·0849	0·0026	79·4	1·3
143-16 s (PP)	857	1574	1·84	14	2·7	100·331	1·621	0·0689	0·0021	62·2	1·0
144-21 s (PP)	452	738	1·63	7	6·9	94·634	1·693	0·1019	0·0034	63·1	1·2
144-22 s (PP)	256	141	0·55	4	17·0	100·412	2·279	0·1816	0·0069	53·1	1·3
144-26 s (PD)	637	76	0·12	5	3·3	120·496	2·091	0·0739	0·0027	51·5	0·9

Table 2: continued

Sample	U (ppm)	Th (ppm)	Th/U	Pb (ppm)	f^{206}Pb (%)	^{238}U/^{206}Pb $\pm$ 1σ (measured)		^{207}Pb/^{206}Pb $\pm$ 1σ (measured)		Age (Ma) $\pm$ 1σ (207-corrected)	
144-26s2 (PP)	1704	3019	1·77	26	0·7	100·766	1·401	0·0529	0·0013	63·2	0·9
144-27 s (SK)	406	13	0·03	4	6·5	114·181	2·308	0·0986	0·0042	52·6	1·1
144-29 s (PP)	683	245	0·36	6	6·4	118·497	2·036	0·0981	0·0032	50·7	0·9

Grain code sample AG144 gives PRI (pristine domain), PP (inclusion-rich porous domain), PD (dense domain in porous zircon) and SK (skeletal domain) according to BSE and CL imaging (Figs 5 and 6).

evolution of Syros, and we will compare the geochronological information obtained from U–Pb on metamorphic zircon with Ar–Ar white mica geochronology.

Pristine zircon generation

Both textural and chemical characteristics suggest a magmatic origin for these zircons. In terms of morphology and chemical composition (e.g. Y/Hf ratio) the plagiogranite zircons are similar to magmatic zircons commonly recovered from oceanic plagiogranites (e.g. Ohnenstetter *et al.*, 1981; Pupin, 1992, 2001; Müller *et al.*, 1996). The development of {100} and lack of {110} prisms, as found on the pristine zircon crystals, seems to be favoured at high magmatic temperatures (Pupin & Turco, 1972). The pristine zircons have medium to high Th/U ratios and many show oscillatory growth zoning, best developed in zircon with xenotime-type coupled substitution from the metagabbro sample. All these features are commonly observed for magmatic zircons (e.g. Rubatto & Gebauer, 1999).

Inclusion populations and textural relationships in the pristine zircons are also consistent with a magmatic origin. In many euhedral zircon grains, apatite occurs as minute needle-shaped inclusions (e.g. Fig. 4c). Both zircon and apatite need a certain degree of melt polymerization (silica activity) to nucleate from a silicate melt, and when the melt is saturated with these phases they commonly co-precipitate. High-pressure minerals were not found as inclusions, at least not unambiguous primary examples, contrary to assertions by Bröcker & Enders (1999, 2001). Whenever high-pressure silicate inclusions were suspected to be primary, i.e. trapped during zircon growth, the zircon in contact invariably showed enhanced luminosity in CL image, suggesting that some re-equilibration has occurred during or after the inclusion has formed. Very often, high-pressure inclusions first suspected to be primary in origin were found, upon close inspection, to be connected to the outside or among each other by healed cracks and secondary fluid inclusion trails. This suggests that silicate inclusions communicated with the 'outside world' during metamorphic overprint. As such, they are poor indicators for a metamorphic origin of their host zircon.

Intergrowth relations of zircon with peak metamorphic phases such as garnet show that the pristine zircon generation pre-dated high-pressure metamorphism. The examples shown in Fig. 11 are from garnet-rich metabasite fragments from the meta-igneous breccia at Grizzas. Garnet growth is syn- to post-tectonic in the blueschist–eclogite-facies mineral parageneses [Grt + Omp + Gln + Ep + Phg + Qtz]. Concentric chemical zonation profiles show a bell-shaped decrease in spessartine component from core to rim matched by an increase in pyrope (e.g. core $Alm_{67}Prp_2Grs_{23}Sps_8$ to rim $Alm_{68}Prp_7Grs_{23}Sps_2$). The patterns are consistent with growth zonation acquired during prograde high-pressure metamorphism. All types of zircon described in this paper occur also as inclusions in garnet. Garnet appears to be chemically stable wherever it is intergrown with the most resorbed zircon. Figure 11 shows that the zircons were already altered before or while they were overgrown by garnet. For this reason, the alteration reactions affecting pristine zircons must date from a time when garnet was either growing or not yet a stable phase.

Trace element contents of the pristine zircon generation, notably the high Y contents, are compelling evidence for a magmatic origin. The solid solution of YPO_4 in $ZrSiO_4$ and vice versa is temperature sensitive (Speer, 1980). Although the solvus between zircon and xenotime has not yet been calibrated for use as a quantitative geothermometer, it is evident that a pristine zircon having about 3 mol % YPO_4 in solid solution, and coexisting with apatite, should be higher temperature in origin than a porous zircon with <1 mol % YPO_4 but saturated with xenotime. Thus, if the paragenesis porous zircon + xenotime formed from pristine zircon at prograde HP/LT metamorphism up to peak temperatures about ~480°C, the type 1 zircon generation must have formed before the high-pressure event,
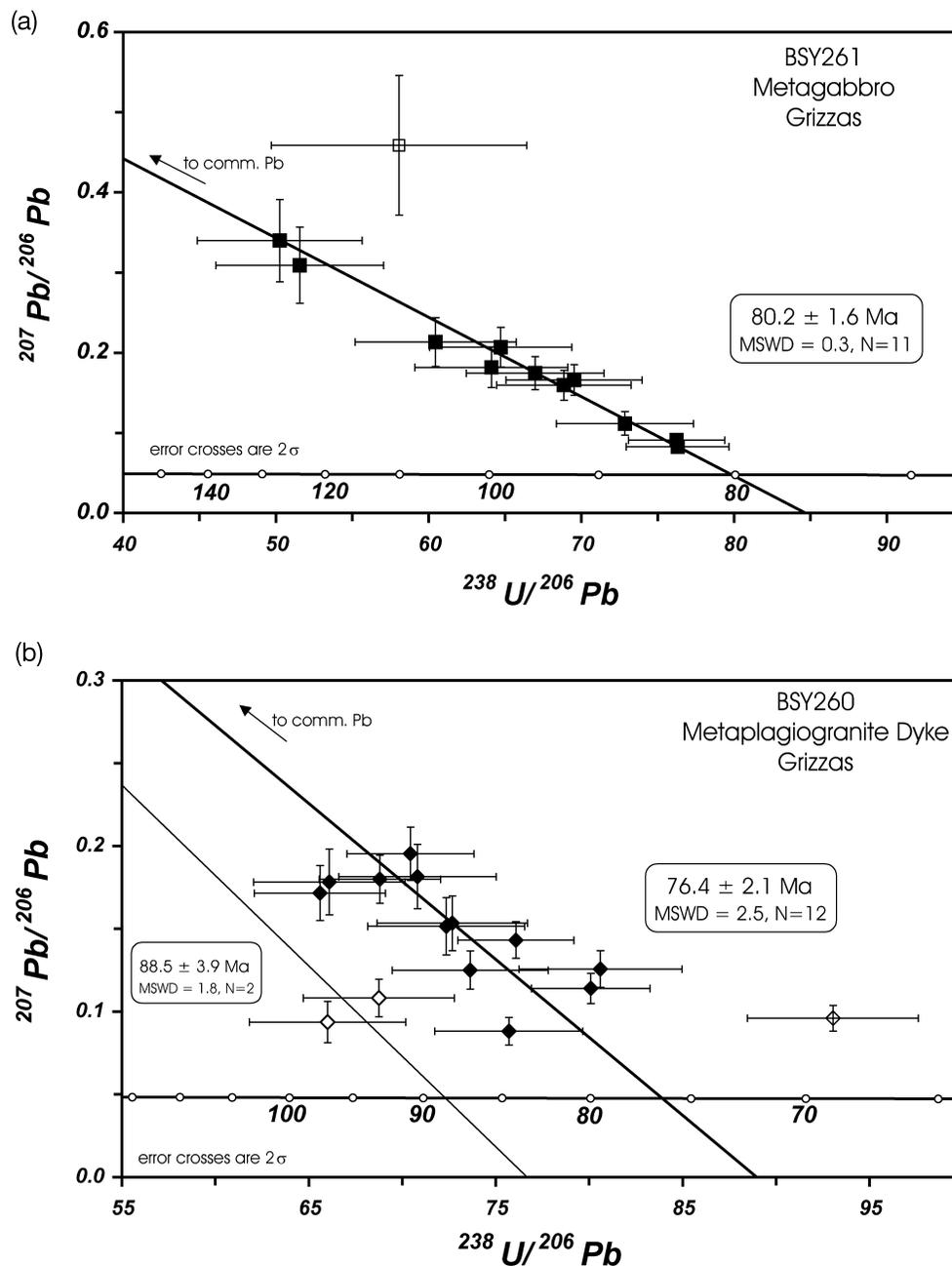
Fig. 9. Isotope ratio plots (Tera–Wasserburg concordia diagrams) of SHRIMP data from zircons interpreted to be igneous in origin. Mean population ages calculated from the concordia intersection of the regression line from common Pb. (a) Pristine zircons from the Grizzas metagabbro, representing a uniform age population. (b) Pristine zircons from the Grizzas meta-plagiogranite dyke, intrusive in the metagabbro; populations divided based on their ages.

and at a temperature suggested higher than 480°C. As there is no petrological evidence for a previous high-temperature event, other than magmatic crystallization, and as all other features of the type 1 zircon generation are compatible with a magmatic origin, we interpret the ages of these zircons to date the magmatic crystallization of the protoliths.

Geochemical data available from the meta-igneous rocks of Syros, although in many respects consistent with magmatic processes, testify to significant post-magmatic element mobility, particularly with respect to Zr (Seck *et al.*, 1996; Bröcker & Enders, 2001; Lagos *et al.*, 2002). Bröcker & Enders (1999, 2001) suggested that their 78 Ma zircon originated during an episode of
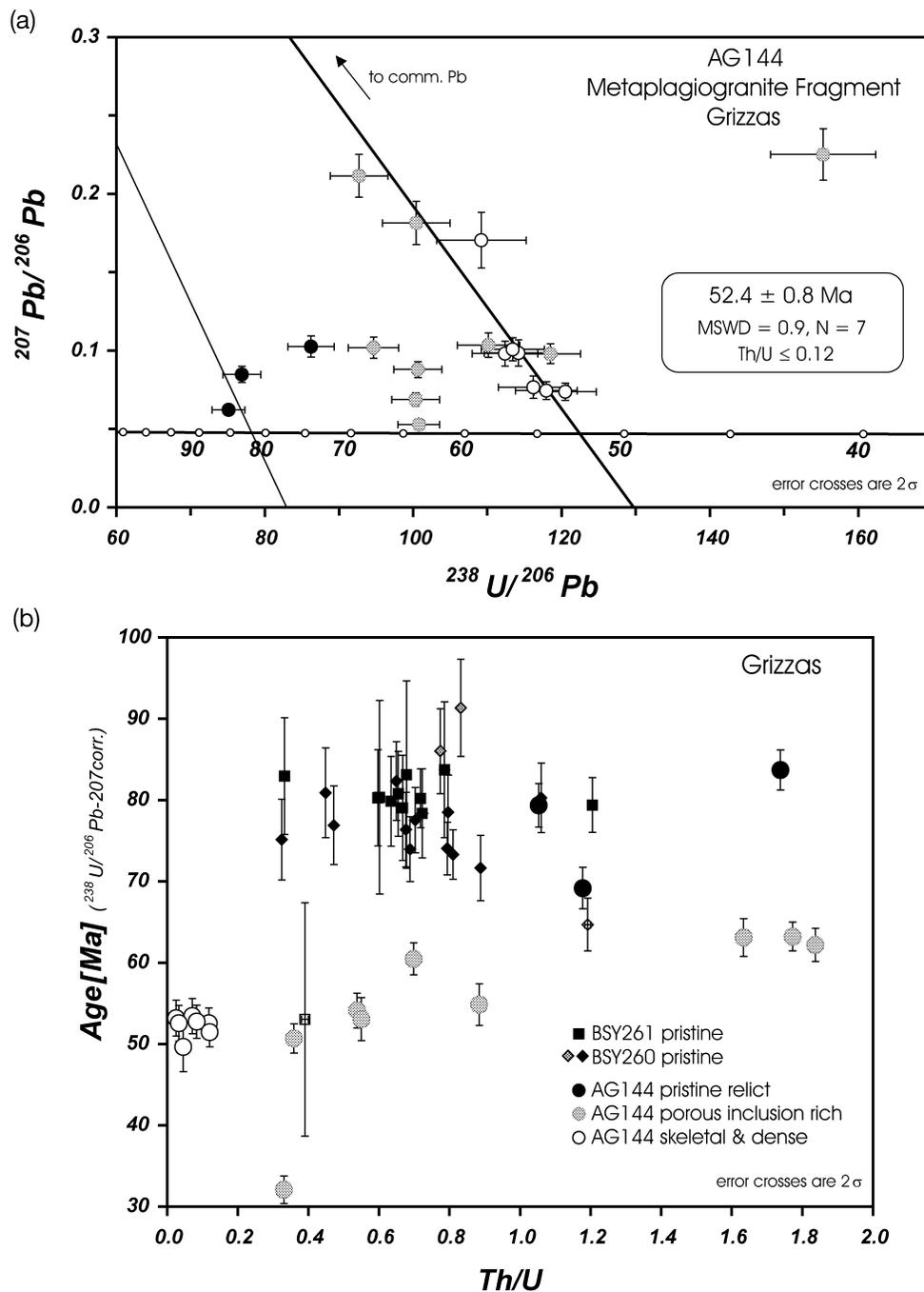
Fig. 10. SHRIMP data obtained on pristine (black), inclusion-rich porous (grey), and skeletal and dense domains in porous zircons (white circles), all from the Grizzas plagiogranite breccia fragment. (a) Tera–Wasserburg diagram; regression through the group of skeletal zircon and zircon domains in the spongy type with the lowest Th/U. (b) Age vs Th/U correlation diagram, to discriminate between old and young zircon generations; all data from Grizzas.

enhanced HFSE mobility at HP/LT metamorphic conditions, which would then have to be Cretaceous in age. From textural and age evidence presented here, it is clear, however, that the pristine Cretaceous zircon generation represents a precursor phase and that zircon derived by recrystallization and Zr remobilization during HP/LT metamorphism is younger. Consequently, the HFSE mobility is likely to be Eocene in age, defined by U–Pb ages of the low-Th/U and skeletal zircons, to be detailed below.
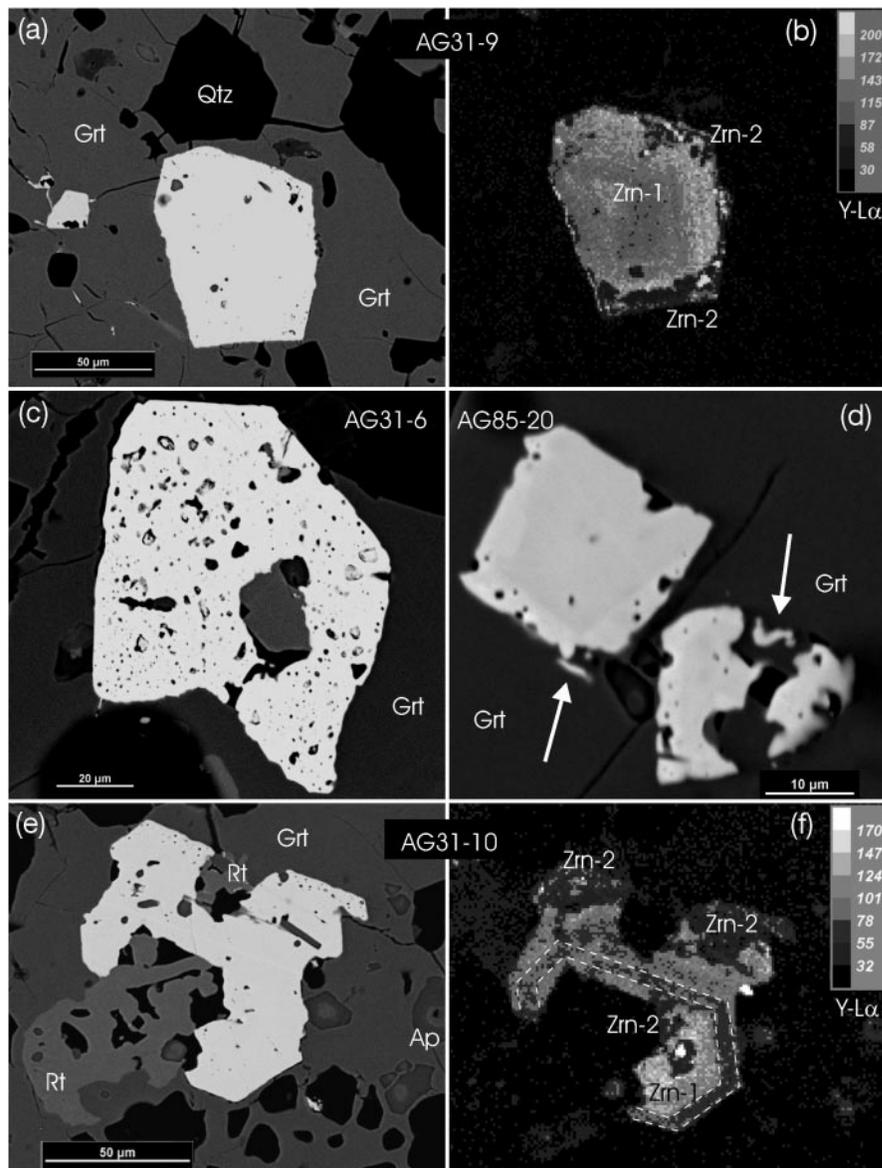
Fig. 11. Zircon inclusions in garnet imaged with BSE and X-ray maps for Y, to identify discrete generations and domains. (a) and (b) Partially recrystallized zircon (type 2); a core with Y growth zonation and a porous rim, low in Y but rich in discrete Y phases (bright spots). (c) Spongy porous zircon (type 3) in BSE image. (d) Skeletal zircon (type 4) in BSE image with delicate zircon–garnet intergrowths. (e) and (f) partially recrystallized and corroded zircon (type 2) in BSE image and corresponding Y distribution map. Corroded curved surfaces are intergrown with garnet, phases present in corrosion pockets are rutile (Rt) and quartz. Dotted lines delineate primary growth zones.

Geochronological interpretation

For reasons outlined above, we conclude that the age of $80 \cdot 2 \pm 1 \cdot 6$ Ma, obtained from the igneous-textured metagabbro zircon, dates magmatic crystallization. In accordance with the intrusive field relations, the younger age at $76 \cdot 4 \pm 2 \cdot 1$ Ma dates the emplacement of the plagiogranite dyke. Some of the isotopic scatter (Fig. 9b), and the distinctively older component ($88 \cdot 5 \pm 3 \cdot 9$ Ma) in the dyke may reflect an inherited zircon component. This agrees with previous results and interpretations of zircons from the same meta-igneous belt, which consistently have magmatic REE patterns (Hoskin & Ireland, 2000) and are similar in type and age (magmatic $74 \cdot 8 \pm 2 \cdot 4$ Ma, and inherited $88 \cdot 8 \pm 8 \cdot 2$ Ma, U–Th–Pb SHRIMP; Keay, 1998). Moreover, including the data of Bröcker & Enders (1999), and Cheney et al. (2000), lithologies from the whole meta-igneous belt on Syros seem cogenetic and homogeneous in age, given that U–Pb geochronology on

pristine zircon all yielded the same ages between 75 and 80 Ma.

Zircon recrystallization and mobilization

The other, younger-generation zircons are a consequence of recrystallization of the pristine, older-generation zircon. Judging from the textures of the composite (type 2) zircon crystals (Figs 5, 7 and 11), the reaction proceeded from the outside to the inside. During reaction, porosity is created, represented by fluid inclusions in the porous zircon shell; trace elements including Y, HREE, Th and P are expelled from the zircon structure and precipitate as discrete phases such as xenotime and (Y,HREE,Th)-silicates; and U−Pb ages are fully or partially reset by Pb loss.

We suggest that the recrystallization process is best defined as dissolution−reprecipitation (O'Neil & Taylor, 1967; Putnis, 2002). Conceptually, we may formulate the process as a conventional, albeit unbalanced, chemical reaction, such as $(Zr,Hf,Y,HREE,Th)(Si,P)O_4 = (Zr,Hf)SiO_4 + (Y,HREE)PO_4 + (Y,HREE,Th)$-silicate. In this reaction, an old, trace element-enriched zircon is the reactant, and young, porous zircon plus xenotime and (Y,HREE,Th)-silicate inclusions are the product phases (Fig. 12). Apatite inclusions are often present in both the educt and product zircon, and can be neglected here. The fluid acts only as a catalyst and solvent, and as such does not partake in the reaction, although remnants of the solvent are trapped as fluid inclusions. A suitable analogy may be considered in the behaviour of salt−water systems. In NaCl-saturated water there does not seem to be any reaction between NaCl and H_2O but only because the dissociation rate of NaCl equals the association rate of NaCl.

With reference to the zircons described, a Y−HREE−Th-enriched zircon, stable at magmatic crystallization, comes in contact with a fluid phase under fundamentally different pressure−temperature conditions. In response to the distinctly different physico-chemical environment, the product zircon can no longer incorporate trace elements to the extent found in the pristine high-temperature zircon generation. Zircon will re-equilibrate and will be replaced by a zircon depleted in minor elements and intergrown with secondary mineral inclusions. An important driving force to promote the reaction may well be the lattice strain resulting from high concentrations (wt % level) of trace elements in solid solution.

During reaction, most of the unstable, trace element enriched zircon is dissolved and reprecipitated directly onto the reaction interface. In consequence, the reactant zircon and product zircon will be single crystals,
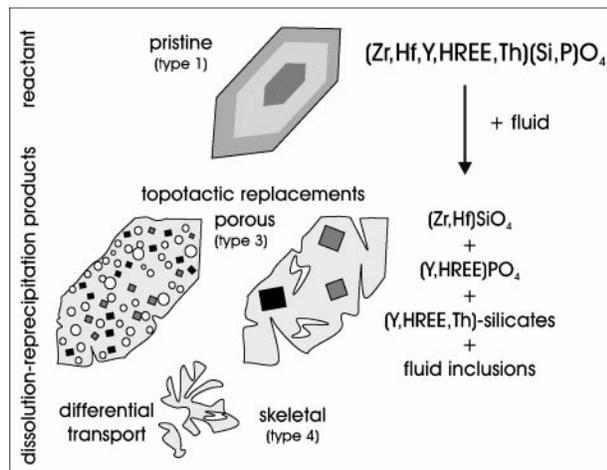

Fig. 12. Schematic diagram showing the principal zircon types recognized, attributed to the dissolution−reprecipitation process described in text.

having the same shape and crystallographic orientation. As the reaction front progresses into trace element-enriched zircon, it precipitates near-pure end-member zircon and insoluble trace elements as inclusion phases. It leaves along its trail a porous structure in which the solvent is occasionally trapped as fluid inclusions. The fluid can be assumed to be saturated with zircon at all times during reaction progress, because solution rate equals precipitation rate. It should be noted that the fluid/rock ratio is irrelevant for the reaction mechanism described. It is only required that the reaction interface be wetted by fluid at all times as long as the reaction proceeds. There is no need for continuous fluid supply from outside sources either, for fluid is not consumed. Also, it should be noted that the fluid does not have to be particularly aggressive toward zircon, although a highly reactive composition would probably accelerate the reaction progress. In natural systems, the time factor does not play the same role as in experimental analogues, where one would probably opt for HF, HCl or alkaline-rich fluids to duplicate the process and accelerate reaction. In particular, in a high-pressure environment, we can expect such a reaction to be very effective, judging from experimental and empirical data. The solubility data by Ayers & Watson (1991) and considerations by Liermann *et al.* (2002) show that Zr solubility in aqueous fluids increases with increasing pressure and rising temperature. Pressure in particular has a marked effect on the solubility of HFSE as shown by Manning (1998); Philippot & Selverstone (1991) provided evidence for Zr mobility from the existence of Zr phases as daughter minerals in fluid inclusions from eclogites.

The dissolution–reprecipitation process described here is probably more widespread than it might appear. Pan (1997) recognized the common association of metamorphic zircon with xenotime and suggested replacement–recrystallization of pre-existing igneous zircon. Putnis (2002) assumed that most mineral replacement and re-equilibration reactions are accomplished by dissolution–reprecipitation, and there is ample direct and indirect evidence to support this view (e.g. O'Neil & Taylor, 1967; Walker *et al.*, 1995). A criterion for dissolution–reprecipitation is the creation of porosity, without which the fluid would be unable to keep contact with the advancing reaction front. Some examples presented here are perhaps unique, because pores at the interface between pristine and recrystallized zircon domains are still preserved and captured *in situ* (e.g. Fig. 7a). These pores, with sizes up to the micrometre scale, may well have served as fluid pathways to accomplish the reaction. However, a dissolution–reprecipitation process may also account for the non-porous recrystallized domains, and for metamorphic zircon rims similar to those discussed by Pidgeon (1992) and Hoskin & Black (2000), assuming that porosity is a transient, ephemeral state hard to preserve through geological time.

Metamictization to aid recrystallization?

It is well known that accumulation of radiation damage in a zircon structure causes macroscopic expansion, and greatly enhances the susceptibility of zircon to alteration and age resetting (e.g. Murakami *et al.*, 1991; Mezger & Krogstad, 1997; Geisler *et al.*, 2001). One might suspect therefore that the porous zircon generation could have been metamict at some time before alteration, to account for volume changes of several percent and the decreased zircon stability. However, none of the zircons described in this paper were ever metamict. The degree of metamictization is usually a function of U and Th concentration and time of radiation exposure, and can be assessed by simple calculation of the accumulated α-dosage the structure will have received (Holland & Gottfried, 1955; Murakami *et al.*, 1991). The time available for metamictization is < 30 Ma if we accept the pristine, 80 Ma zircon as reactant and the 52 Ma domains in the porous zircon as the products in the dissolution–reprecipitation process outlined above. U and Th concentrations such as in the pristine domain illustrated in Fig. 5b (1000 and 1745 ppm, respectively) accumulate, within 30 Ma, an α-dosage less than 0.2×10^{18} α-decay events/g. This is only one-tenth of the amount necessary to initiate noticeable changes in a typical zircon structure (e.g. Holland & Gottfried, 1955; Murakami *et al.*, 1991). Obviously, radiation damage did not play an important role in enhancing

the reactivity of zircon, and the high porosity is simply caused by material loss during the replacement process. It is evident that also non-metamict zircon may be highly reactive, especially when trace element contents are high (e.g. Görz & White, 1970; Köppel & Sommerauer, 1974; Pidgeon, 1992; Schaltegger *et al.*, 1999; Hoskin & Black, 2000).

Geochronological interpretation

The highly porous and inclusion-rich (type 3) zircon domains invariably include an admixture of relict zircon, fluid inclusions and newly formed crystalline phases that might well be capable of incorporating radiogenic Pb. In addition, high porosity might create large surfaces and pathways for fluids to leach out Pb at any time. Although a replacement reaction could have been initiated at any time after magmatic emplacement, if it was induced or at least facilitated by high concentrations in trace elements, we consider the wide range in U–Th–Pb results obtained on the inclusion-rich zircon domains to be erratic, not reflecting a meaningful geological age.

More meaningful in terms of geological history is the skeletal (type 4) generation. Porous and skeletal types invariably occur together in the same samples, and skeletal zircon and dense domains within porous type are identical in age. The skeletal zircons, besides minor overgrowth rims, may account for material that is lost into the fluid during the replacement of trace element enriched zircon, and reprecipitated outside the parent grain. Along with the inclusion-poor domains of the porous zircon, the skeletal zircons define a tight cluster in U–Pb ages of 52.4 ± 0.8 Ma and Th/U ratios of ≤ 0.1. Their texture is dense and they lack fine inclusions, and they are unlikely to contain relicts of an older zircon generation. Therefore, they lack the possibility that the SHRIMP analyses may be compromised by incomplete Pb loss or contamination by unidentified domains.

The presence of pores and corrosional features, the skeletal zircon generation and overgrowth rims, as well as bulk chemical data (see Bröcker & Enders, 1999, 2001) show that at times Zr was a mobile element. Judging from intergrowth relations with garnet and the considerations outlined above, we assume that maximum Zr mobility in the samples described coincided with high-pressure peak metamorphic conditions. We suggest that dissolution, transport and reprecipitation out of a fluid phase, referred to here as dissolution–reprecipitation, were simultaneous processes, and that the U–Pb ages of the skeletal zircons, along with pure domains in the porous zircons, closely date peak metamorphism of the Eocene blueschist–eclogite-facies overprint, at 52.4 ± 0.8 Ma. This
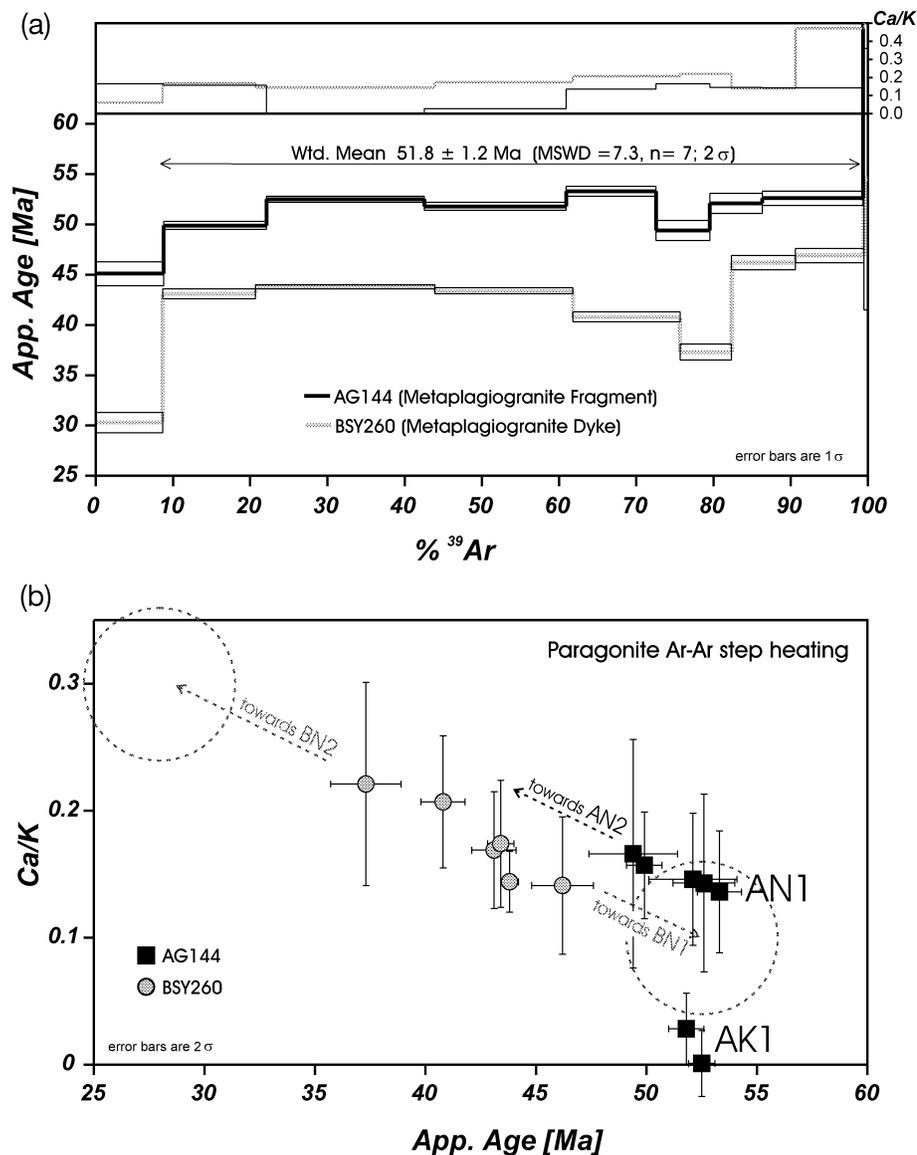
Fig. 13. Ar–Ar step heating results. (a) Age spectra from paragonite separates of the plagiogranite dyke (BSY260) and the breccia fragment sample (AG144). (b) Correlation between Ca/K and apparent ages for the steps degassed at medium temperatures. The triangular distribution suggests a mixture of the Ar reservoirs AN1/BN1, AK1 and AN2/BN2, described in text. Dotted circles indicate probable end-members according to EMPA analyses.

proposition is supported by excellent agreement of the U−Pb ages with Ar−Ar white mica ages, as described below.

Ar–Ar white mica geochronology

To evaluate the metamorphic ages given by the skeletal zircon generation, we analysed white mica concentrates from the meta-plagiogranite dyke and the meta-plagiogranite breccia fragment using the Ar−Ar step heating method. Both samples recrystallized in the Jd−Qtz stability field. In the breccia sample, the paragenesis Jd + Pg + Qtz ± Czo ± Phg is well preserved, whereas in the dyke sample Jd is largely replaced by retrograde Ab. Electron microprobe analyses identified two chemically distinct Pg generations: N1, with Pg enriched in phengite component; N2, with Pg closer to end-member composition. K_2O contents are between $\sim$0·8 and 0·3 wt %, and both contain minor concentrations of CaO (margarite component). Decrease in phengite component causes Ca/K in Pg to increase. In some cases, Pg of both samples is intergrown with Phg.

An additional retrograde K-rich phase occurs as minute scales in the Ab-rich coronas replacing Jd, and is lost during separation of the coarse-grained mica population.

Figure 13a shows the degassing spectra of two paragonite concentrates from the dyke and the breccia sample. Both spectra are discordant, show similar humps in shape, and steps yield apparent ages of 30–54 Ma. The least retrogressed breccia sample yields the oldest apparent ages. The weighted mean of the largely flat part of this spectrum yields an age about 52 Ma. The interpretation is more detailed with application of heterochemical mixture principles, taking into account age and chemical correlations. Upon heating, hydrous minerals collapse and, depending on mineral chemical composition, release Ar over a very restricted temperature range (Sletten & Onstott, 1998). The Ar release temperature depends on chemical composition because the latter influences the average bond length and strength (Dahl, 1996), and thus the *in vacuo* breakdown. Element ratios calculated from the Ar isotopic compositions provide a tool to resolve the components that degas in a polyphase mixture (e.g. Villa *et al.*, 1997, 2000).

Figure 13b shows the Ca/K ratio and the apparent ages obtained from each step, excluding the lowest and highest temperature fractions (likely to represent impurities, as indicated by high Cl/K and high Ca/K ratios). In this figure, AG144 is seen to be composed of two Ar reservoirs at least: AN1, a *c.* 52 Ma old Pg with medium Ca/K ratios; AK1, a *c.* 52 Ma old Phg with lowest Ca/K. Sample BSY260 gives younger step ages, which can be interpreted as due to the degassing of two Ar reservoirs (see Villa, 2001): BN1, an old Pg with Ca/K $\sim$ 0·1; BN2, a young Pg with Ca/K $\sim$0·3. The mixing of these two reservoirs produces a linear array (grey circles). In principle, the age of the two reservoirs can be obtained from the x values of the mixing line that correspond to the y values at compositions measured by electron microprobe analysis (EMPA). Limited by the error of EMPA analyses, the older Pg (BN1) may have the same age as reservoirs AN1 and AK1, and the younger Pg (BN2) may date from retrograde overprint at $\leq$30 Ma. An additional Phg component does not contribute significant mass to be obvious in the Ca/K age correlation. A similar mixture of two Pg reservoirs (AN1, AN2) is also suggested to account for the scatter in the Pg component of sample AG144. An isochron can be calculated from cogenetic phases; we therefore considered only the steps from the unretrogressed Pg and Phg components and obtain an isochron age of 52·3 $\pm$ 0·7 Ma (2σ, $n = 5$, MSWD = 1·6, intercept $^{40}Ar/^{36}Ar$ = 295·7 $\pm$ 3·2).

This age is in excellent agreement with the U–Pb age of 52·4 $\pm$ 0·8 Ma defined by the skeletal and low-Th/U zircon generation from the same sample. It also agrees well with Ar–Ar white mica ages of 50–54 Ma reported from blueschist–eclogite-facies samples elsewhere on Syros (Maluski *et al.*, 1987; Baldwin, 1996). In the absence of recrystallization, white micas retain their Ar well above the temperature reached during blueschist–eclogite-facies metamorphism (Hammerschmidt & Frank, 1991; Hames & Cheney, 1997; Villa, 1998; De Sigoyer *et al.*, 2000; Di Vincenzo *et al.*, 2001). We therefore suggest that both the white micas and the metamorphic zircons from Syros date crystallization close to the peak of Eocene HP/LT metamorphism.

CONCLUSIONS

(1) Meta-igneous rocks of Syros carry several generations of zircon that are related to each other by dissolution–reprecipitation processes. One zircon end-member is a pristine zircon generation with well-developed growth zoning, high Th/U ratios and elevated contents in trivalent cations. The other end-member has skeletal crystal shapes, low Th/U and negligible trace element contents. Between these end-members there is a range of zircon textures that show complex inclusion populations and variable progress of a replacement–recrystallization process, attributed to the re-equilibration of zircon at HP/LT metamorphic conditions.

(2) The two end-members are distinct in terms of SHRIMP U–Pb age. The pristine generation yields an age of 80·2 $\pm$ 1·6 Ma from a metagabbro and 76·4 $\pm$ 2·1 Ma from a plagiogranite dyke. The skeletal and low-Th/U generation gives a tight age cluster at 52·4 $\pm$ 0·8 Ma. Between these end-members, analyses on mixed domains result in highly variable and erratic ages.

(3) We agree with Keay (1998) and Hoskin & Ireland (2000) that the ages between 75 and 80 Ma date the magmatic emplacement of the protoliths. All features of this zircon generation, including zonation patterns, high trace element contents and reactive intergrowth relations with peak metamorphic silicate phases, point toward a magmatic origin. The skeletal and low-Th/U zircon generation precipitated from a metamorphic fluid phase, and may mark maximum HFSE mobility in a high-pressure metamorphic fluid. The U–Pb zircon age of 52·4 $\pm$ 0·8 Ma is in excellent agreement with the Ar–Ar white mica age of 52·3 $\pm$ 0·7 Ma obtained from paragonite concentrates of the same samples. Both the Ar–Ar and the U–Pb systems are interpreted to date peak conditions of the Eocene high-pressure/low-temperature event. There is no geochronological evidence for a pre-Eocene high-pressure metamorphic event in the north of Syros.

(4) The rocks from which the zircons are derived originally belonged to a segment of short-lived oceanic crust, situated at a Late Cretaceous convergent plate margin. Whereas remnants of a contemporaneous high-temperature belt are preserved in the Cycladic Upper Unit, evidence for Cretaceous high-pressure metamorphism in the Cyclades has yet to be found.

ACKNOWLEDGEMENTS

SUPPLEMENTARY DATA

Supplementary data for this paper are available on *Journal of Petrology* online

REFERENCES

Altherr, R., Schliestedt, M., Okrusch, M., Seidel, E., Kreuzer, H., Harre, W., Lenz, H., Wendt, I. & Wagner, G. A. (1979). Geochronology of high-pressure rocks on Siphnos (Cyclades, Greece). *Contributions to Mineralogy and Petrology* **70**, 245–255.

Altherr, R., Kreuzer, H., Wendt, I., Lenz, H., Wagner, G. A., Keller, J., Harre, W. & Höhndorf, A. (1982). A late Oligocene/early Miocene high temperature belt in the Attic–Cycladic Crystalline Complex (SE Pelagonian, Greece). *Geologisches Jahrbuch, Reihe E* **23**, 97–164.

Altherr, R., Kreuzer, H., Lenz, H., Wendt, I., Harre, W. & Dürr, S. (1994). Further evidence for a late Cretaceous low-pressure/high-temperature terrane in the Cyclades, Greece. *Chemie der Erde* **54**, 319–328.

Andriessen, P. A. M., Boelrijk, N. A. I. M., Hebeda, E. H., Priem, H. N. A., Verdumen, E. A. T. & Verschure, R. H. (1979). Dating the events of metamorphism and granitic magmatism in the Alpine orogen of Naxos (Cyclades, Greece). *Contributions to Mineralogy and Petrology* **69**, 215–255.

Ayers, J. C. & Watson, E. B. (1991). Solubility of apatite, monazite, zircon, and rutile in supercritical aqueous fluids with implications for subduction zone geochemistry. *Philosophical Transactions of the Royal Society of London, Series A* **335**, 365–375.

Baldwin, S. L. (1996). Contrasting $P–T–t$ histories for blueschists from the western Baja terrane and the Aegean: effects of synsubduction exhumation and backarc extension. *Geophysical Monograph, American Geophysical Union* **96**, 135–141.

Baldwin, S. L. & Lister, G. S. (1998). Thermochronology of the South Cyclades shear zone, Ios, Greece: effects of ductile shear in the argon partial retention zone. *Journal of Geophysical Research, Solid Earth* **103**, 7315–7336.

Belluso, E., Ruffini, R., Schaller, M. & Villa, I. M. (2000). Electron-microscope and Ar isotope characterization of chemically heterogeneous amphiboles from the Palala shear zone, Limpopo Belt, South Africa. *European Journal of Mineralogy* **12**, 45–62.

Black, L. P., Kinny, P. D. & Sheraton, J. W. (1991). The difficulties of dating mafic dykes: an Antarctic example. *Contributions to Mineralogy and Petrology* **109**, 183–194.

Bonneau, M., Geyssant, J., Kienast, J.-R., Lepvrier, C. & Maluski, H. (1980). Tectonique et métamorphisme Haute Pression d'âge éocène dans les Hellénides: exemple de l'île de Syros (Cyclades, Grèce). *Comptes Rendus de l'Académie des Sciences, Série D* **291**, 171–174.

Bröcker, M. & Enders, M. (1999). U–Pb zircon geochronology of unusual eclogite-facies rocks from Syros and Tinos (Cyclades, Greece). *Geological Magazine* **136**, 111–118.

Bröcker, M. & Enders, M. (2001). Unusual bulk-rock compositions in eclogite-facies rocks from Syros and Tinos (Cyclades, Greece): implications for U–Pb zircon geochronology. *Chemical Geology* **175**, 581–603.

Bröcker, M., Kreuzer, H., Matthews, A. & Okrusch, M. (1993). $^{40}Ar/^{39}Ar$ and oxygen isotope studies of polymetamorphism from Tinos Island, Cycladic blueschist belt, Greece. *Journal of Metamorphic Geology* **11**, 223–240.

Cheney, J. T., Schumacher, J. C., Coath, C. D., Brady, J. B., DiFillipo, E. L., Argyrou, E. N., Otis, J. W., Sperry, A. J. & Sable, J. E (2000). Ion microprobe ages of zircons from blueschists, Syros, Greece. *Geological Society of America, Abstracts with Programs* **32**, 152.

Cherniak, D. J., Hanchar, J. M. & Watson, E. B. (1997). Rare-earth diffusion in zircon. *Chemical Geology* **134**, 289–301.

Claoué-Long, J. C., King, R. W. & Kerrich, R. (1990). Archaean hydrothermal zircon in the Abitibi greenstone belt: constraints on the timing of gold mineralisation. *Earth and Planetary Science Letters* **98**, 109–128.

Claoué-Long, J. C., Compston, W., Roberts, J. & Fanning, C. M. (1995). Two Carboniferous ages: a comparison of SHRIMP zircon dating with conventional zircon ages and $^{40}Ar/^{39}Ar$ analysis. In: Berggren, W. A., Kent, D. V., Aubry, M. P. & Hardenbol, J. (eds) *Geochronology Time Scales and Global Stratigraphic Correlation. SEPM (Society for Sedimentary Geology) Special Publication* **54**, 3–21.

Compston, W., Williams, I. S. & Meyer, C. (1984). U–Pb geochronology of zircons from lunar breccia 73217 using a sensitive high mass-resolution ion microprobe. *Journal of Geophysical Research B* **89**(Supplement), B525–B534.

Cumming, G. L. & Richards, J. R. (1975). Ore lead isotope ratios in a continuously changing Earth. *Earth and Planetary Science Letters* **28**, 155–171.

Dahl, P. S. (1996). The crystal-chemical basis for Ar retention in micas: inferences from interlayer partitioning and implications for geochronology. *Contributions to Mineralogy and Petrology* **123**, 22–39.

De Sigoyer, J., Chavagnac, V., Blichert-Toft, J., Villa, I. M., Luais, B., Guillot, S., Cosca, M. & Mascle, G. (2000). Dating the Indian continental subduction and collisional thickening in the northwest Himalaya: multichronology of the Tso Morari eclogites. *Geology* **28**, 487–490.

Di Vincenzo, G., Ghiribelli, B., Giorgetti, G. & Palmeri, R. (2001). Evidence of a close link between petrology and isotope records: constraints from SEM, EMP, TEM and in situ ^{40}Ar–^{39}Ar laser analyses on multiple generations of white micas (Lanterman Range, Antarctica). *Earth and Planetary Science Letters* **192**, 389–405.

Dixon, J. E. (1976). Glaucophane schists of Syros, Greece. *Bulletin de la Société Géologique de France, Série 7* **18**, 280.

Dixon, J. E. & Ridley, J. (1987). Syros. In: Helgeson, H. C. (ed.) *Chemical Transport in Metasomatic Processes. NATO Advanced Study Institutes Series* **C 218**, 489–501.

Dürr, S. (1986). Das Attisch-kykladische Kristallin. In: Jacobshagen, V. (ed.) *Geologie von Griechenland. Beiträge zur regionalen Geologie der Erde* **19**, 116–149.

Finch, R. J., Hanchar, J. M., Hoskin, P. W. O. & Burns, P. C. (2001). Rare-earth elements in synthetic zircon: Part 2. A single-crystal X-ray study of xenotime substitution. *American Mineralogist* **86**, 681–689.

Geisler, T., Ulonska, M., Schleicher, H., Pidgeon, R. T. & van Bronswijk, W. (2001). Leaching and differential recrystallization of metamict zircon under experimental hydrothermal conditions. *Contributions to Mineralogy and Petrology* **141**, 53–65.

Görz, H. & White, E. W. (1970). Minor and trace elements in HF-soluble zircons. *Contributions to Mineralogy and Petrology* **29**, 180–182.

Hames, W. E. & Cheney, J. T. (1997). On the loss of $^{40}Ar^*$ from muscovite during polymetamorphism. *Geochimica et Cosmochimica Acta* **61**, 3863–3872.

Hammerschmidt, K. & Frank, E. (1991). Relics of high pressure metamorphism in the Lepontine Alps (Switzerland)—^{40}Ar–^{39}Ar and microprobe analyses on white K-micas. *Schweizerische Mineralogische und Petrographische Mitteilungen* **71**, 261–274.

Hanchar, J. M. & Miller, C. F. (1993). Zircon zonation patterns as revealed by cathodoluminescence and backscattered electron images: implications for interpretation of complex crustal histories. *Chemical Geology* **110**, 1–13.

Hanchar, J. M., Finch, R. J., Hoskin, P. W. O., Watson, E. B., Cherniak, D. J. & Mariano, A. N. (2001). Rare earth elements in synthetic zircon: Part 1. Synthesis and rare earth element and phosphorus doping. *American Mineralogist* **86**, 667–680.

Hecht, J. (1984). *Geological map of Greece 1:50 000, Syros Island*. Athens: Institute of Geology and Mineral Exploration (IGME).

Hinton, R. W. & Upton, B. G. J. (1991). The chemistry of zircon: variations within and between large crystals from syenite and alkali basalt xenoliths. *Geochimica et Cosmochimica Acta* **55**, 3287–3302.

Holland, H. D. & Gottfried, D. (1955). The effect of nuclear radiation on the structure of zircon. *Acta Crystallographica* **8**, 291–300.

Hoskin, P. W. O. & Black, L. P. (2000). Metamorphic zircon formation by solid-state recrystallization of protolith igneous zircon. *Journal of Metamorphic Geology* **18**, 423–439.

Hoskin, P. W. O. & Ireland, T. R. (2000). Rare earth element chemistry of zircon and its use as a provenance indicator. *Geology* **28**, 627–630.

Hoskin, P. W. O., Kinny, P. D., Wyborn, D. & Chappell, B. W. (2000). Identifying accessory mineral saturation during differentiation in granitoid magmas: an integrated approach. *Journal of Petrology* **41**, 1365–1396.

Keay, S. (1998). The geological evolution of the Cyclades, Greece: constraints from SHRIMP U–Pb geochronology. Ph.D. thesis, Australian National University, Canberra, 335 pp.

Keay, S. Lister, G. & Buick, I. (2001). The timing of partial melting, Barrovian metamorphism and granite intrusion in the Naxos metamorphic core complex, Cyclades, Aegean Sea, Greece. *Tectonophysics* **342**, 275–312.

Köppel, V. & Sommerauer, J. (1974). Trace elements and the behaviour of the U–Pb system in inherited and newly formed zircons. *Contributions to Mineralogy and Petrology* **43**, 71–82.

Kötz, J. (1989). Zur Geochemie der Metabasite von Syros, Kykladen, Griechenand. Ph.D. thesis, Universität Köln, 182 pp.

Kretz, R. (1983). Symbols for rock-forming minerals. *American Mineralogist* **68**, 277–279.

Lagos, M., Münker, C., Tomaschek, F. & Ballhaus, C. (2002). Geochemistry and Lu–Hf-geochronology of the metavolcanic Grizzas sequence in northern Syros (Cyclades, Greece). *Beihefte zum European Journal of Mineralogy* **14**(1), 97.

Lee, J. K. W., Williams, I. S. & Ellis, D. J. (1997). Pb, U and Th diffusion in natural zircon. *Nature* **390**, 159–162.

Liati, A. & Gebauer, D. (1999). Constraining the prograde and retrograde P–T–t path of Eocene HP rocks by SHRIMP dating of different zircon domains: inferred rates of heating, burial, cooling and exhumation for central Rhodope, northern Greece. *Contributions to Mineralogy and Petrology* **135**, 340–354.

Liermann, H. P., Isachsen, C., Altenberger, U. & Oberhänsli, R. (2002). Behavior of zircon during high-pressure, low-temperature metamorphism: case study from the Internal Unit of the Sesia Zone (Western Italian Alps). *European Journal of Mineralogy* **14**, 61–71.

Lips, A. L., White, S. H. & Wijbrans, J. R. (1998). ^{40}Ar/^{39}Ar laserprobe direct dating of discrete deformational events: a continuous record of early Alpine tectonics in the Pelagonian Zone, NW Aegean area, Greece. *Tectonophysics* **298**, 133–153.

Ludwig, K. R. (1999). Isoplot/Ex 2.06 a geochronological toolkit for Microsoft Excel. *Berkeley Geochronology Center Special Publication* **1a**, 1–49.

Maluski, H., Bonneau, M. & Kienast, J.-R. (1987). Dating the metamorphic events in the Cycladic area: ^{39}Ar/^{40}Ar data from metamorphic rocks of the island of Syros (Greece). *Bulletin de la Société Géologique de France* **8**, 833–842.

Manning, C. E. (1998). Fluid composition at the blueschist–eclogite transition in the model system Na_2O–MgO–Al_2O_3–SiO_2–H_2O–HCl. *Schweizerische Mineralogische und Petrographische Mitteilungen* **78**, 225–242.

Mezger, K. & Krogstad, E. J. (1997). Interpretation of discordant U–Pb zircon ages: an evaluation. *Journal of Metamorphic Geology* **15**, 127–140.

Müller, B., Klötzli, U., Schaltegger, U. & Flisch, M. (1996). Early Cambrian oceanic plagiogranite in the Silvretta Nappe, eastern Alps: geochemical, zircon U–Pb and Rb–Sr data from garnet–hornblende–plagioclase gneisses. *Geologische Rundschau* **85**, 822–831.

Murakami, T., Chakoumakos, B. C., Ewing, R. C., Lumpkin, G. R. & Weber, W. J. (1991). Alpha-decay event damage in zircon. *American Mineralogist* **76**, 1510–1532.

Ohnenstetter, M., Ohnenstetter, D., Vidal, P., Cornichet, J., Hermitte, D. & Mace, J. (1981). Crystallization and age of zircon from Corsican ophiolitic albitites: consequences for oceanic

expansion in Jurassic times. *Earth and Planetary Science Letters* **54**, 397–408.

Okrusch, M. & Bröcker, M. (1990). Eclogites associated with high-grade blueschists in the Cycladic archipelago, Greece: a review. *European Journal of Mineralogy* **2**, 451–478.

O'Neil, J. R. & Taylor, H. P., Jr (1967). The oxygen isotope and cation exchange chemistry of feldspars. *American Mineralogist* **52**, 1414–1437.

Pan, Y. (1997). Zircon- and monazite-forming metamorphic reactions at Manitouwadge, Ontario. *Canadian Mineralogist* **35**, 105–118.

Philippot, P. & Selverstone, J. (1991). Trace-element-rich brines in eclogitic veins: implications for fluid composition and transport during subduction. *Contributions to Mineralogy and Petrology* **106**, 417–430.

Pidgeon, R. T. (1992). Recrystallisation of oscillatory zoned zircon: some geochronological and petrological implications. *Contributions to Mineralogy and Petrology* **110**, 463–472.

Pidgeon, R. T., Fufaro, D., Kennedy, A. K., Nemchin, S., van Bronswjk, W. & Todt, W. A. (1994). Calibration of zircon standards for the Curtin SHRIMP II. *US Geological Survey Circular* **117**, 251.

Pupin, J. P. (1992). Les zircons des granites océaniques et continentaux: couplage typologie–géochimie des éléments en traces. *Bulletin de la Société Géologique de France* **163**, 495–507.

Pupin, J. P. (2001). Granite genesis related to geodynamics from Hf–Y in zircon. *Geological Society of America, Special Paper* **350**, 245–256.

Pupin, J. P. & Turco, G. (1972). Une typologie originale du zircon accessoire. *Bulletin de la Société Française de Minéralogie et de Cristallographie* **95**, 348–359.

Putlitz, B., Matthews, A. & Valley, J. W. (2000). Oxygen and hydrogen isotope study of high-pressure metagabbros and metabasalts (Cyclades, Greece): implications for the subduction of oceanic crust. *Contributions to Mineralogy and Petrology* **138**, 114–126.

Putnis, A. (2002). Mineral replacement reactions: from macroscopic observations to microscopic mechanisms. *Mineralogical Magazine* **66**, 689–708.

Reinecke, T., Altherr, R., Hartung, B., Hatzipanagiotou, K., Kreuzer, H., Harre, W., Klein, H., Keller, J. & Geenen, E. (1982). Remnants of a Late Cretaceous high temperature belt on the island of Anafi (Cyclades, Greece). *Neues Jahrbuch für Geologie und Paläontologie, Abhandlungen* **145**, 157–182.

Ridley, J. (1982). Tectonic style, strain history, and fabric development in a blueschist terrain, Syros, Greece. Ph.D. thesis, University of Edinburgh, 283 pp.

Ridley, J. (1984). Evidence of a temperature-dependent 'blueshist' to 'eclogite' transformation in high-pressure metamorphism of metabasic rocks. *Journal of Petrology* **25**, 852–870.

Robinson, K., Gibbs, G. V. & Ribbe, P. H. (1971). The structure of zircon: a comparison with garnet. *American Mineralogist* **56**, 782–790.

Rubatto, D. (2002). Zircon trace element geochemistry: partitioning with garnet and the link between U–Pb ages and metamorphism. *Chemical Geology* **184**, 123–138.

Rubatto, D. & Gebauer, D. (1999). Use of cathodoluminescence for U–Pb zircon dating by ion microprobe: some examples from the Western Alps. In: Pagel, M., Barbin, V., Blanc, P. & Ohnenstetter, D. (eds) *Cathodoluminescence in Geosciences*. Berlin: Springer, pp. 373–400.

Rubatto, D., Gebauer, D. & Compagnoni, R. (1999). Dating of eclogite-facies zircons: the age of Alpine metamorphism in the Sesia–Lanzo Zone (Western Alps). *Earth and Planetary Science Letters* **167**, 141–158.

Rubin, J. N., Henry, C. D. & Price, J. G. (1989). Hydrothermal zircons and zircon overgrowths, Sierra Blanca Peaks, Texas. *American Mineralogist* **74**, 865–869.

Saxena, S. K. (1966). Evolution of zircons in sedimentary and metamorphic rocks. *Sedimentology* **6**, 1–33.

Schaltegger, U., Fanning, C. M., Günther, D., Maurin, J. C., Schulmann, K. & Gebauer, D. (1999). Growth, annealing and recrystallization of zircon and preservation of monazite in high-grade metamorphism: conventional and in-situ U–Pb isotope, cathodoluminescence and microchemical evidence. *Contributions to Mineralogy and Petrology* **134**, 186–201.

Schermer, E. R., Lux, D. R. & Burchfield, B. C. (1990). Temperature–time history of subducted continental crust, Mount Olympos Region, Greece. *Tectonics* **9**, 1165–1195.

Seck, H. A., Kötz, J., Okrusch, M., Seidel, E. & Stosch, H.-G. (1996). Geochemistry of a meta-ophiolite suite: an association of metagabbros, eclogites and glaucophanites on the island of Syros, Greece. *European Journal of Mineralogy* **8**, 607–623.

Sletten, V. W. & Onstott, T. C. (1998). The effect of the instability of muscovite during *in vacuo* heating on $^{40}Ar/^{39}Ar$ step-heating spectra. *Geochimica et Cosmochimica Acta* **62**, 123–141.

Speer, J. A. (1980). Zircon. In: Ribbe, P. H. (ed.) *Orthosilicates. Mineralogical Society of America, Reviews in Mineralogy* **5**, 67–112.

Steiger, R. H. & Jäger, E. (1977). Subcommission on Geochronology: convention on the use of decay constants in geo- and cosmochronology. *Earth and Planetary Science Letters* **36**, 359–362.

Tomaschek, F., Baumann, A., Villa, I. M., Kennedy, A. & Ballhaus, C. (2000). Geochronological constraints on a Cretaceous metamorphic event from the Vari Unit (Syros, Cyclades, Greece). *Beihefte zum European Journal of Mineralogy* **12**(1), 214.

Tomaschek, F., Kennedy, A., Keay, S. & Ballhaus, C. (2001). Geochronological constraints on Carboniferous and Triassic magmatism in the Cyclades: SHRIMP U–Pb ages of zircons from Syros, Greece. *Journal of Conference Abstracts* **6**(1), 315.

Trotet, F., Vidal, O. & Jolivet, L. (2001). Exhumation of Syros and Sifnos metamorphic rocks (Cyclades, Greece). New constraints on the $P–T$ paths. *European Journal of Mineralogy* **13**, 901–920.

Vavra, G., Gebauer, D., Schmid, R. & Compston, W. (1996). Multiple zircon growth and recrystallization during polyphase Late Carboniferous to Triassic metamorphism in granulites of the Ivrea Zone (Southern Alps): an ion microprobe (SHRIMP) study. *Contributions to Mineralogy and Petrology* **122**, 337–358.

Vavra, G., Schmid, R. & Gebauer, D. (1999). Internal morphology, habit and U–Th–Pb microanalysis of amphibolite-to-granulite facies zircons: geochronology of the Ivrea Zone (Southern Alps). *Contributions to Mineralogy and Petrology* **134**, 380–404.

Villa, I. M. (1998). Isotopic closure. *Terra Nova* **10**, 42–47.

Villa, I. M. (2001). Radiogenic isotopes in fluid inclusions. *Lithos* **55**, 115–124.

Villa, I. M., Ruggieri, G. & Puxeddu, M. (1997). Petrological and geochronological discrimination of two white-mica generations in a granite cored from the Lardello–Travale geothermal field (Italy). *European Journal of Mineralogy* **9**, 563–568.

Villa, I. M., Hermann, J., Münterer, O. & Trommsdorff, V. (2000). $^{39}Ar–^{40}Ar$ dating of multiply zoned amphibole generations (Malenco, Italian Alps). *Contributions to Mineralogy and Petrology* **140**, 363–381.

Walker, F. D. L., Lee, M. R. & Parsons, I. (1995). Micropores and micropermeable texture in alkali feldspars: geochemical and geophysical implications. *Mineralogical Magazine* **59**, 505–534.

Wijbrans, J. R. & McDougall, I. (1986). $^{40}Ar/^{39}Ar$ dating of white micas from an Alpine high-pressure metamorphic belt on Naxos (Greece): the resetting of the argon isotopic system. *Contributions to Mineralogy and Petrology* **93**, 187–194.

Wijbrans, J. R., Schliestedt, M. & York, D. (1990). Single grain argon laser probe dating of phengites from the blueschist to greenschist transition on Sifnos (Cyclades, Greece). *Contributions to Mineralogy and Petrology* **104**, 582–593.

Williams, I. S. & Claesson, S. (1987). Isotopic evidence for the Precambrian provenance and Caledonian metamorphism of high grade paragneisses from the Seve Nappes, Scandinavian Caledonides. II. Ion microprobe zircon U–Th–Pb. *Contributions to Mineralogy and Petrology* **97**, 205–217.

Williams, I. S., Buick, I. S. & Cartwright, I. (1996). An extended episode of early Mesoproterozoic metamorphic fluid flow in the Reynolds Range, central Australia. *Journal of Metamorphic Geology* **14**, 29–47.

Woodhead, J. A., Rossman, G. R. & Thomas, A. P. (1991). Hydrous species in zircon. *American Mineralogist* **76**, 1533–1546.